Problems of Planetology, Cosmochemistry and Meteoritica

Barenbaum A.A. Virtual-corpuscular mechanism of gravity in space and its effect on light photons and Sun motion in Galaxy.

UDC 539.12

OGRI RAS azary@mail.ru

Abstract. The author has previously shown that Newton's law of universal gravitation, acting instantly at a distance, has a virtual-corpuscular nature. The attraction of bodies in this law is physically carried out by elementary particles – gravitons, which are massless virtual vector bosons. Mathematically adequately, attraction is described by a tensor in vector space, the rank of which is generally determined by the number of bodies that create an attractive force at each point of physical space in accordance with Newton's law of gravitation. This mechanism is involved in studying the action of gravitational fields in space on light photons and on the Sun motion in Galaxy. In the first case, this mechanism explains the redshifts in Hubble's law and the cosmic microwave background origin. And in the second, using Newton's law of universal gravitation, a model was created that allows us to construct a single stratigraphic scale for the Phanerozoic and Precambrian and to clarify the Galaxy spiral structure.

Keywords: *Newton's law of universal gravitation, virtual-corpuscular mechanism of gravitation, Hubble's law of redshifts, galactic model of geological cyclicity.*

Introduction. Based on the analysis of results of the research of S.E. Shnol (2009) and the experiments of N.A. Kozyrev (1991), which revealed the influence of Sun, Moon, planets of Solar System and nearby stars on near-Earth gravitational field, we previously concluded (Barenbaum, 2024, 2024a, 2024b, 2025c) that the physical mechanism of attraction in Newton's law of universal gravitation is "virtual-corpuscular". The attraction in Newton's law, acting instantly at all distances, is physically created by gravitons, which are massless virtual vector bosons. The energy of gravitons is $\sim 10^{-4}$ eV, frequency is $\sim 10^{9}$ sec^{-1} and their lifetime is $\sim 10^{-9}$ sec. Gravitons do not "fly" to Earth from space, but create the force of attraction of interacting bodies directly in the bodies themselves in their place.

Mathematically adequately, the virtual-corpuscular Newtonian attraction mechanism is described by a tensor in the vector field of gravity, the rank of which is determined by the number of bodies that instantly create an attractive force at each point in physical space according to Newton's law of gravity. Moreover, in many cases it is possible to limit oneself to taking into account the attractive forces of only the bodies of interest. When bodies move from one point in physical space to another, the change in the gravitational field occurs in quantum jumps.

It is obvious that virtual-corpuscular mechanism of gravity acts differently on micro- and macro-objects. Its action in space is considered using two examples. In the first example, we discuss the interaction of light photons with cosmic gravitational fields. This mechanism allows us to explain the red shifts of light in the Hubble law and to offer a different physical explanation for the cosmic microwave background (CMB) origin, an alternative to the one accepted in cosmology. In the second example, we use the instantly acting virtual-corpuscular mechanism of gravity to calculate the parameters of Sun's orbit in Galaxy based on astronomical and geological data.

Example 1: Hubble's Law and Cosmic Microwave Background. To substantiate the possibility of solving cosmological problems using the virtual-corpuscular mechanism of gravity, the author constructed two theoretical models (Barenbaum, 2018, 2019, 2021, and 2025). The first model (Barenbaum, 2018) explains the red shifts in the Hubble law by the fact that when interacting with gravitational fields on the way to Earth, photons lose energy, emitting low-energy electromagnetic quanta. The process continues until the photon energy decreases to the temperature of outer space $T = 2.725$ K. As a result, on the one hand, the light from distant sources "reddens", and on the other, low-energy quanta are formed, which are the cosmic microwave background. The model allows us to measure the average density of matter in space and establish that this matter is stars participating in the cosmochemical circulation of baryonic substance in the Metagalaxy.

This cosmochemical circulation is studied by the second model (Barenbaum, 2019), which explains the energy spectrum of cosmic microwave radiation (Smoot, 1992) by the participation of gravitons. The model shows that the circulation is accompanied by the destruction of "old" stars in galaxies and the formation of "young" OB stars of high luminosity from their gas and dust products. The circulation process is in dynamic equilibrium at the space temperature $T = 2.725$ K. At this temperature, the energy density released during the synthesis of ^{4}He from ^{1}H in OB stars and emitted by them in the optical range coincides with energy density of cosmic microwave background. We have obtained this conclusion based on results of the works of E. Regener (1933) and G. Burbidge and F. Hoyle (1998). The first measured the energy flux of optical radiation from stars in the night sky and determined the temperature of outer space from it $T \approx 2.8$ K. The second authors concluded that light chemical

elements (D, ^{3}He, ^{6}Li, ^{7}Li, ^{9}Be, ^{10}B and ^{11}B) were not formed at the moment of a cosmological explosion, but were synthesized from hydrogen, like ^{4}He, in OB stars over the past ~100 billion years.

The parameters of the cosmochemical cycle of baryonic matter in space, calculated according to our first and second models (Barenbaum, 2025) and explaining the parameters of CMB radiation measuring by the COBE station (Wikipedia) are given in Table 1.

Table 1: The parameters of cosmochemical circulation

Parameters of outer space at with the Hubble constant H_o = 67 km/s/ Mpc	Parameter value
Average density of baryonic matter	7.7×10^{-23} kg/m^3
Concentration of "old" stars with a mass of (0.5 M_Θ)	~3×10^{-3} pc^{-3}
Concentration of "young" OB stars with a mass of (50 M_Θ)	~1.5×10^{-7} pc^{-3},
Ratio of concentrations of "young" and "old" stars	~ 2×10^{-4}
Light flux of OB stars near Earth (Regener, 1933)	3.53×10^{-3} erg ·cm^{-2}·s^{-1}
Density of energy emitted by OB stars (Burbidge, Hoyle, 1998)	4.37×10^{-13} erg/cm^3
Energy density of the CMB (Smoot, 1992)	4.2×10^{-13} erg /cm^3
Average energy of CMB photons (Smoot, 1992)	6×10^{-4} eV
Lifetime of "young" OB stars in galaxies	5×10^{7} years
Lifetime of "old" stars in the Metagalaxy	~10^{13} years
Average time of circulation and life of galaxies	~10^{13} years

The parameters of the circulation (Table 1) allow us to conclude (Barenbaum, 2025):

1. The Hubble redshift law and background microwave radiation are consequences of the cosmochemical circulation of baryonic matter caused by formation and death of stars and galaxies during the circulation.

2. With the Hubble constant H_o = 67 km/s/Mpc, the process of cosmochemical circulation is in a state of thermodynamic equilibrium at an average temperature of outer space T = 2.725 K.

3. The average temperature of outer space T = 2.725 K is uniquely determined by characteristic period of circulation of ~10^{13} years and ratio of young OB and "old" stars participating in it, which is equal to 2×10^{-4}.

Example 2: Galactic model of geological cyclicity. The applicability of virtual-corpuscular mechanism of gravity for stars will be demonstrated using the example of calculating Sun's orbit parameters in Galaxy using the galactic model of geological cyclicity (Barenbaum, 2010, 2022; Barenbaum, Titorenko 2020). This model made it possible to explain the key geological events in Earth history by bombardments of our planet by galactic comets at the moments of Sun's entry into Galaxy jet streams and spiral arms. The latest version of model has been tested in refining Galaxy spiral structure and determining its gravitational potential based on Sun's orbit parameters, as well as in constructing geochronological scale of Phanerozoic and Precambrian (Barenbaum, 2022).

The version of galactic model (Barenbaum and Titorenko, 2020) projected onto Galaxy plane is shown in Fig. 1, and in Fig. 2 the times of Sun's entry into Galaxy jet streams and spiral arms calculated using the model for the last 600 mln years are compared with the boundaries of periods and eras of Phanerozoic geochronological scale.

In this model version, our Galaxy has 4 identical arms of electromagnetic nature, twisted into logarithmic spirals (I–IV), which rotate as a whole around Galaxy center with a period of T_G = 200 mln years, and 2 gas-dust jet streams (1 and 2), twisted into Archimedes spirals. Both streams flow out at a speed of 300 km/s tangentially from opposite points of the rapidly rotating nuclear disk of Galaxy. The disk is inclined to galactic plane at an angle of 20° and precesses with a period of its rotation T_d = 50 mln years. The matter flowing out of disk fan-shapely spreads in disk plane, condensing into comets and stars. The condensation processes are most active in arms at a distance of the corotation radius R* from center, where the radii of curvature of logarithmic and Archimedes spirals coincide.

Calculations show that after its emergence in arm IV at a distance R* from center, Sun moves along an elliptical orbit, the line of apses of which rotates around center in forward direction with a period of T_α = 2 billion years. At the same time, Sun makes small-amplitude oscillations across galactic plane with a period of T_Z = 50 mln years. When moving along its orbit, Sun crosses the arms and jet streams of Galaxy after 20-37 mln years, and then for a period of ~1-5 mln years all planets are subjected to bombardments by galactic comets.

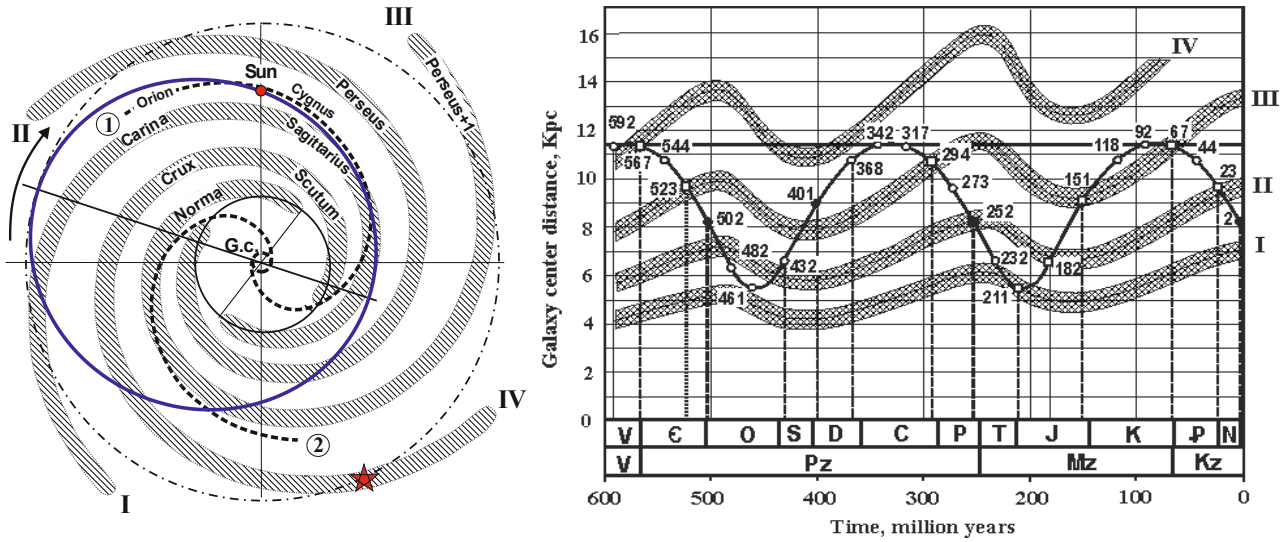

Fig. 1. The Galaxy spiral structure and the Sun position in orbit (ellipse) in projection onto galactic plane in the modern era. The stripes are the spiral galactic arms; the dotted lines are two Archimedean jet streams. The asterisk is the place in arm IV where Solar System was formed earlier

Fig. 2. Changes in Sun's position relative to Galaxy center and its spiral arms over time. The dots with numbers on Sun's orbit indicate the times (million years) when Sun entered jet streams. Below is the Phanerozoic geochronological scale with its boundaries of ranks of systems and eras

On Earth, all such events are reflected in the Phanerozoic stratigraphic scale in the form of its boundaries, the rank of which is determined by the intensity of cometary bombardments (Fig. 2). The times of most intense bombardments determine the boundaries of eras and eras, less intense ones – the boundaries of systems, and weak ones – the boundaries of divisions. The boundaries of the divisions correspond to Sun's hits in jet streams, the boundaries of systems – to its hits simultaneously in jet streams and spiral galactic arms, and the same hits at R^* determine the boundaries of Paleozoic (Pz) and Cenozoic (Kz) eras. For the Mesozoic (Mz), this rule is not fulfilled, and geologists attribute this boundary to a very intense cometary bombardment at the P/T boundary.

It should be emphasized that the calculation accuracy of the boundaries of Phanerozoic scale and parameters of Galaxy spiral structure is generally higher than that of geology and astronomy data used in developing the galactic model. At the same time, high calculation accuracy is achieved only under the condition that Sun orbital motion is in resonance with the rotation of arms and Galaxy nuclear disk. So, during one revolution of apsidal line of its orbit, Sun makes 8 full revolutions along orbit and 9 revolutions around the center, while Galaxy and its nuclear disk make 10 and 80 revolutions, and Sun makes 80 oscillations across galactic plane. It should also be noted (Barenbaum, 2022a, 2023) that in resonance with rotation period of apsidal line of solar orbit T_α = 2 billion years, the ecliptic plane of Solar System also precesses.

It hardly needs proof that in classical mechanics such a multi-frequency resonance requires instantaneous action of Newton's law of gravitation simultaneously in the entire Galaxy. The discussed virtual-corpuscular physical mechanism of gravitation satisfies this requirement.

Conclusion

1. It is shown that the virtual-corpuscular physical mechanism of Newton's attraction with participation of virtual gravitons acts instantly at all distances.

2. Newton's virtual-corpuscular mechanism of attraction is equally applicable to both microscopic objects and stellar mass objects.

References

Barenbaum A.A. (2010) Galactocentric paradigm in geology and astronomy. – Moscow: LIBROKOM. 2010. 546 p.

Barenbaum A.A. (2018) The nature of redshifts in the spectra of distant galaxies // Engineering Physics, No 6, Pp.18-23. DOI: 10.25791/infi zik.06.2018.044

Barenbaum A.A. (2019) Origin of the cosmic microwave background // Engineering Physics. No 1, Pp.39-48. DOI: 10.25791/infi zik.01.2019.392.

Barenbaum A.A. (2021) Hubble's Law and the Cosmic Microwave Background in the Absence of the Big Bang // Book: Research Trends and Challenges in Physical Science. V.4, Pp. 119-130.

Barenbaum A.A. (2022) Solution of Problem Questions of Astronomy and Geology Using the Optimized Galactic Model // Book: Physical and Mathematical Modeling of Earth and Environment Processes–2022. V.E. Karev (Ed.) DOI: 10.1007/978-3-031-25962-3.

Barenbaum A.A. (2022a) Measuring the precession period of Solar System ecliptic plane using galactic model // The 13 Moscow Solar System Symposium, October 10-14, 2022, Book of abstracts Space Research Inst. RAS. Moscow. Poster 13MS3-GP-PS-04, Pp. 211-214.

Barenbaum A.A. (2023) On the issue of "True polar wander" Phenomenon and Its Alternative Physical Interpretation Based on Galactic Model // Book: Processes in GeoMedia – Volume VII. (Springer). T. Chaplina (Ed.) pp. 49-69. DOI: 10.1007/978-981-99-6575-5.

Barenbaum, A.A. (2024) Discussion of S.E. Shnol's experiments: detection of corpuscular properties of the near-Earth gravitational field // Proceedings of VESEMPG-2024.– Moscow: GEOKHI RAS. Pp. 221-226.

Barenbaum, A.A. (2024a) Discussion of S.E. Shnol's experiments: detection of corpuscular properties of gravity, discovery of gravitons and the physical nature of gravity // Proceedings of the X international scientific conference: Physical and mathematical modeling of processes in geomedia. – Moscow: IPMech RAS. Pp. 56-61.

Barenbaum, A.A. (2024b) On the mechanism of Newton's gravitational attraction and the physical nature of gravity // Proceedings of the VIII Russian conference: Foundations of fundamental physics and mathematics (OFFM-2024). – Moscow: RUDN. Pp. 154-159.

Barenbaum A.A. (2025) Experiments of S. Shnol, the Physical Nature of Gravitation, Hubble's Law and Cosmic Microwave Background Radiation // Springer Nature Switzerland AG. V. Karev (Ed.): PMMEEP 2023, SPEES, Pp.1–20, 2025. https://doi.org/10.1007/978-3-031-88459-7_48

Barenbaum A.A., Titorenko A.S. (2020) Galactic model of geological cyclicity: optimization of parameters and testing using geological and astronomical data // Proceedings of VESEMPG-2020. - M: GEOKHI RAS, Pp. 210-215.

Burbidge G., Hoyle F. (1998) The origin of helium and other light elements // Astrophysical Journal. №1, 509, L1–L3.

Kozyrev N.A. (1991) Selected Works / Compiled by A.N. Dadaev, L.S. Shikhobalov. – Leningrad. Leningrad University, 448 p.

Regener E. (1933) The Energy Flux of Cosmic Rays // Zeitschrift für Physik. V.80, Pp. 666-669.

Shnol S.E. (2009) Cosmophysical factors in random processes. – Stockholm: Svenska fysikarkivet, 388 p.

Smoot G.F. et al. (1992) Structure in the COBE differential microwave radiometer first-year maps // Astrophysical Journal Letters, V.396, L1-L5

Basilevsky A.T.[1], Krasilnikov A.S.[1], Li Yuan[2], Michael G.G.[3] Surface morphology of three permanently shadowed and two normally illuminated floors of lunar craters. *UDC 523.3*

[1] Vernadsky institute RAN, 119991, Moscow, Russia, *atbas@geokhi.ru*, *krasilnikov_a.s.@geokhi.ru*; [2] Suzhou Vocational University, SuZhou, 215009, China, *YuanLi_SciRes@outlook.com*; [3] CAS Institute of Geochemistry, Guizhou, China, gregory@mail.gyig.ac.cn.

Abstract. On the example of three near-polar craters and two craters on the middle latitudes the corresponding surface morphology of permanently shadowed and normally illuminated floors of these craters has been studied. Under study were near-polar craters Faustini, Shoemaker and Haworth and the middle-latitude craters Macrobius and Boss. It was found that the surface morphology of all five studied craters is dominated by impact (meteoritic) craters with diameters from several to several hundreds of meters. For the floors of craters of Macrobius and Boss the presence of gentle-sloped hills is also typical. On the floors of the near-polar craters small craters with "lobate" rims are observed, that probably indicate the presence in the target material of significant content of water ice.

***Keywords**: The Moon, craters, permanently shadowed floors, normally-illuminated floors, regolith, water ice.*

With the help of photogeologic analysis of images taken by ShadowCam and LROC NAC cameras and with involvement of data of measurements by laser altimeter LOLA, the surface morphology of permanently shadowed floors of the near-polar craters Faustini (81.18° S., 84.31° E., D = 42.5 km), Shoemaker (88.14° S., 84.31° E., D = 51 km) and Haworth (87.45° S., 5.17° E., D = 51 km) and normally illuminated floors of the middle-latitude craters Macrobius (21.26° N., 84.31° N., D = 63 km) and Boss (45.75° N., 84.31° E., D = 50 km) was studied. It was shown that on the floors of all five craters under study the surface morphology is dominated by craters with diameters from several to several hundred meters. On the floors of craters Macrobius and Boss gentle-sloped hills are observed, which are absent on the floors of craters Faustini, Shoemaker and Haworth. So the floors of the studied near-polar craters in the scale of several kilometers are flatter. On the floors of the near-polar craters, craters with 'lobate' rims are observed, the morphology of which looks somewhat similar to the 'lobate' morphology typical of endings of ejecta from craters of Mars. Formation of such rims is probably due to presence of significant content of H_2O ice in the target material. Such craters comprise a few percent of the total number considered. They are distributed in different places of the study areas and differ in size. Possibly, this indicates that water ice in the target material is distributed inhomogeneously in area and in the depth of occurrence. On the floors of craters Macrobius and Boss craters with the 'lobate' morphology of their rims one are rarely observed. This observation demands the further study.

Comparative study of surface morphology of permanently shadowed and normally illuminated by Sun areas of lunar surface was recently done on the example of the floor of crater Shoemaker and the

areas of operation of Lunokhod-1 and Apollo-16 (Basilevsky, Li, 2024). But taking into account the specifics of accumulation of regolith in topographic depressions, which are zones of positive balance (see, e.g., Basilevsky et al., 2020), it is interesting to compare the surface morphology in similar geomorphological situations, in this case, on the floors of craters with diameters of several tens of kilometers.

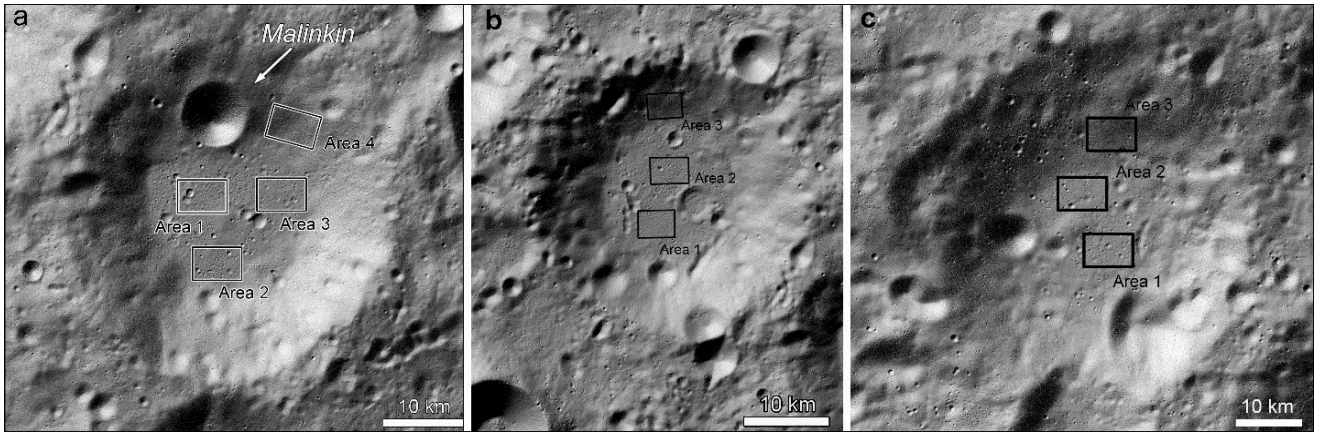

Fig. 1. a) general view of crater Faustini with study areas; b) general view of crater Shoemaker with study areas; c) general view of crater Haworth with study areas. The images are hill-shade ones (Vereshchaka and Kovaleva, 2016) based on digital terrain models.

It is seen in Figure 1, that the permanently shadowed floors of the three considered craters are generally plain-like. The study areas on them are 4.5 x 6 km and are located on approximately horizontal surfaces of these floors outside of craters with diameter more than one kilometer and relatively large positive landforms.

In Figure 2a is shown the ShadowCam image of study area 1 on the floor of crater Faustini. It is seen that the surface morphology here is determined by presence of craters with diameters from tens to hundreds of meters. In the left part of the area is a crater with diameter of 1140 m with the 'lobate' morphology of its rim (Fig. 2b).

In Figure 2 the surface relief with domination of impact (meteorite) craters with diameters of tens and hundreds of meters is seen. In the left part of Fig. 2a a crater (D = 1140 m) with the 'lobate' rim is seen. This is a crater with the most prominent (among those studied by us) rim morphology of this type. Firstly, this given crater was described in the work of Robinson et al. (2024), in which they suggested a possible cause of such rim morphology – the presence of significant concentrations of water ice in the target material. Within the study areas on the floors of craters Faustini, Shoemaker and Haworth the number of craters with diameter ≥150 m with the 'lobate' rim morphology varies from 3 to 9. Within the study areas, craters with the 'lobate' rim are distributed inhomogeneously, that probably suggests an uneven distribution of water ice in the target.

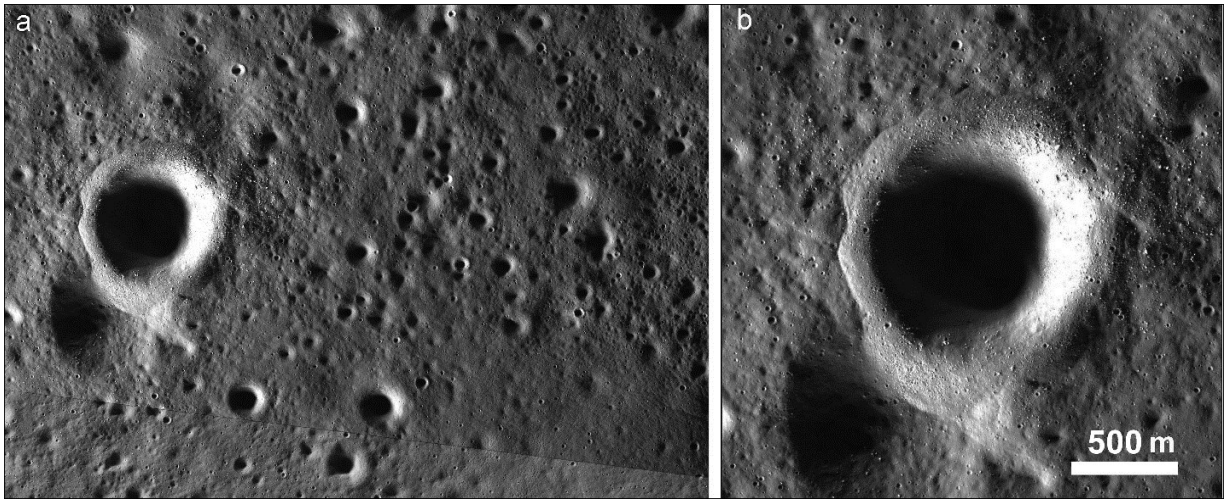

Fig. 2. a) the ShadowCam image of Study area 1 on the floor of crater Faustini; b) the detailed view of the crater with 'lobate' rim**.**

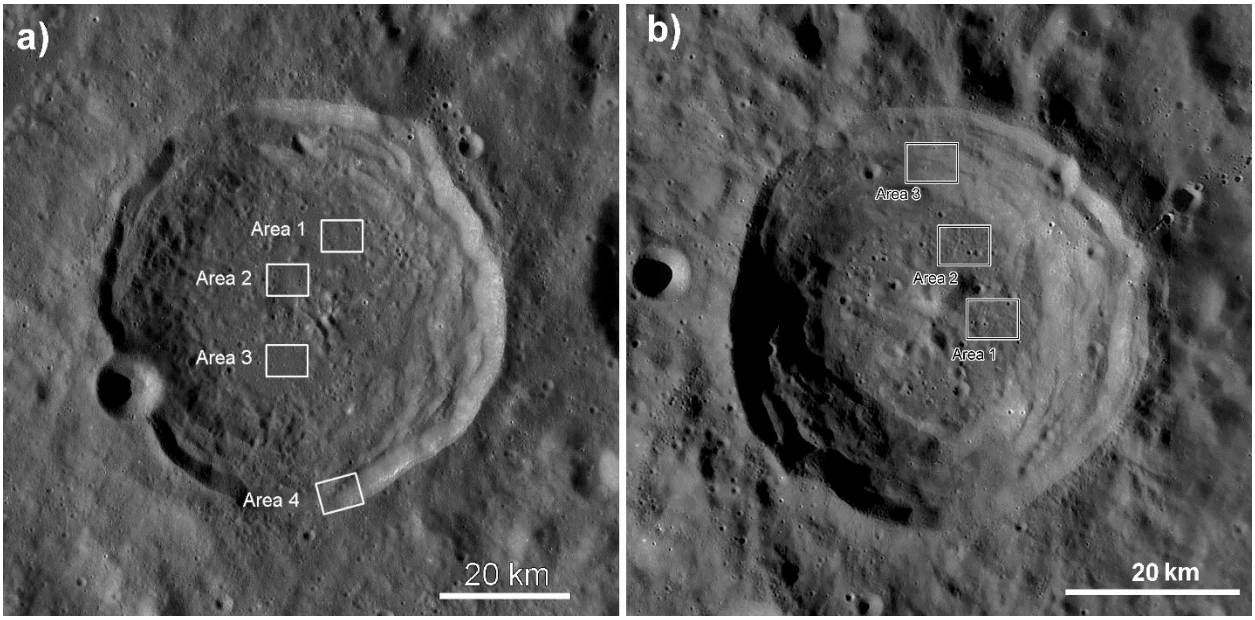

Fig. 3. a) general view of crater Macrobius with Study areas; b) general view of crater Boss with Study areas; mosaic of images WAC_GLOBAL_E300N0450_1350_100M.

It is seen in Fig. 3 that surface of floors of craters Macrobius and Boss is a plain complicated by hills from hundreds of meters to 3-5 km and craters with diameters smaller than 2 km. Besides, crater Boss has a central peak of 5 x 6 km across slightly displaced from the crater center to the north.

In Fig. 4a the ShadowCam image of study area 2 on the floor of crater Boss is shown. It is seen that surface morphology is determined here by presence of craters with diameters tens to hundreds of meters. Besides, several gentle-sloped hills on which these craters are superposed are seen.

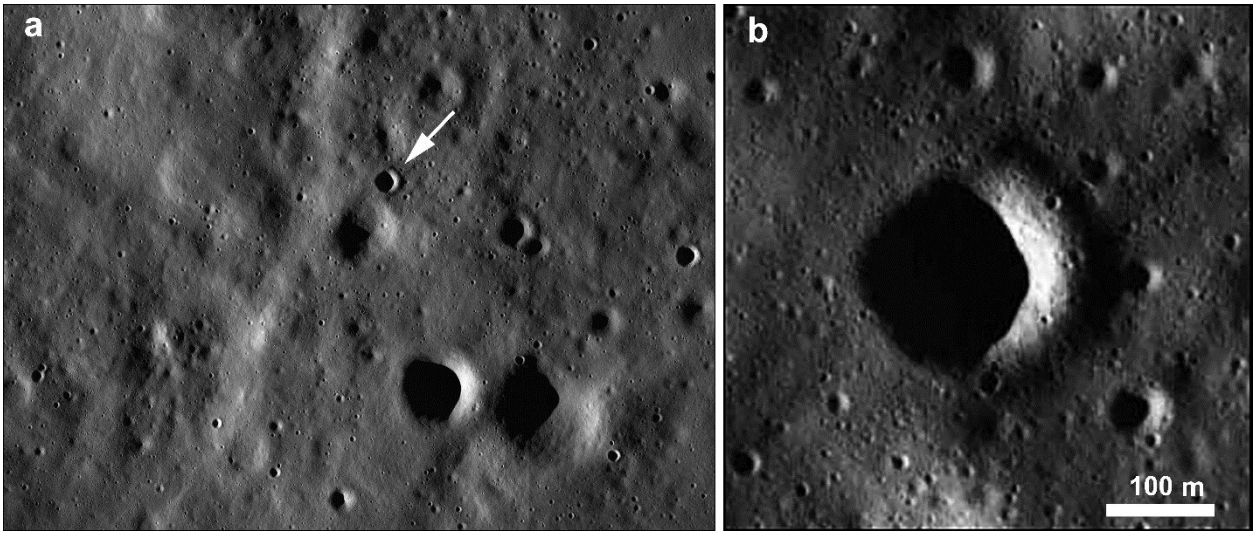

Fig. 4. a) ShadowCam image of study area 2 on the floor of crater Boss; b) detailed image of the crater with diameter 217 m (arrow in Fig. 4a), the rim morphology of which resembles the 'lobate' one.

In Fig. 4 a relief of the surface with domination of impact (meteorite) craters with diameters from tens to hundreds of meters and several gentle-sloped hills is seen. Among craters with diameters ≥150 m are sometimes observed those whose rim morphology resembles the 'lobate' one. Their number within the study areas varies from one to three.

From the data presented above it follows that in the surface morphology of the floors of the five studied craters impact craters dominate with diameters from tens to hundreds of meters. So, the dominating process of surface reworking, both in permanently shadowed and normally illuminated, is meteorite bombardment. On the floors of craters Macrobius and Boss gentle-sloped hills are observed which are absent on the floors of the near-pole craters. The age of the three considered near-polar craters is Pre-Nectarian (Tye et al., 2015), while age of crater Macrobius is Early Imbrian (Wilhelms et

al., 1987) and age of crater Boss is Late Imbrian (Lunar Impact Crater Database, 2009−2011). Probably, the absence of the gentle-sloped hills on the floors of the near-pole craters is due to flattening the primary relief of the floors of impact craters with diameters of a few tens of kilometers by arrival of fragmental material of ejecta from the close and distant craters. Meanwhile the intensity of bombardment of the Moon in the Pre-Nectarian time was much higher than in the Imbrian period and correspondingly the arrival of material of ejecta from other craters into the near-polar craters considered by us was much higher than into craters Macrobius and Boss.

Sources of funding: The work was done under the GEOKHI RAS state assignment (A.T. Basilevsky and A.S. Krasilnikov) and supported by Suzhou Vocational University (Yuan Li) and CAS Institute of Geochemistry (G.G. Michael).

References

1. Basilevsky A.T. and Li Yuan. Surface morphology inside the PSR area of lunar polar crater Shoemaker in comparison with that of the sunlit areas. Planet. and Space Science. 2024, V. 241. 105839. 10 p.
2. Basilevsky A.T., Michael G.G., Krasilnikov S.S., Kozlova N.A. The destruction of small lunar craters. Solar System Research. 2020. V. 54, No 5, 361-371.
3. Robinson M.S., Mahanti P., Bussey D.B.J and 11 co-authors. Seeing in the shadows // 55th Lunar and Planet. Sci. Conf. 2024. Abstract 1669.
4. Tye A.R., Fassett, C.I., Head, J.W., and 5 co-authors., 2015. The age of lunar south circumpolar craters Haworth, Shoemaker, Faustini, and Shackleton. Icarus 255, 70–77.
5. Wilhelms D.E., McCauley J.F, Trask N.J. The geologic history of the Moon. USGS Professional Paper 1348. 1987.
6. Lunar Impact Crater Database, 2009−2011.
7. Vereschaka T.V., Kovaleva O.V. Imaging of relief on maps. M.: Scientific world, 2016. 184 p. (in Russian).

Glazovskaya L.I. Planar deformations in zircon from impactites and conditions of their formation. *UDC 552+550.42*

M.V. Lomonosov Moscow State University, Department of Geology, Moscow *Liudmilaglazov@yandex.ru*

Abstract . The formation of planar microstrutures (PDFs) in impactites has been studied.. Planar microstrutures have been identified in zircons of varying degrees of transformation: in zircon containing reidite (a high-density modification of zircon), in zircon with zones of decomposition into ZrO_2 and SiO_2, in zircon containing granular rims and in zircon with a melted rims.

Keywords: *impactites, zircon, reidite, planar microstrutures, granular textures, melted glasses.*

Planar microstrutures (or, as is russian literature, planar elements) refer to the diaplect transformations of minerals in impactites. Planar microstrutures (PDFs) are closed structures (unlike planar cracks) that represent zones of optical disturbances and degeneracy of the crystalline state along the sliding planes of the blocks of the crystal lattice. relative to each other under the impact compression. The orientation of the planar microstrutures depends on the degree of impact compression. Planar microstrutures are narrow (1-2 microns) and frequent (2-5 microns) zones of reduced birefringence, which are arranged in series. There are zones of more weakly deformed matter between them. Planar microstrutures are observed in two or three directions, most often up to 5 directions, but there are steadily recurring and 10 directions.

The directions of planar microstrutures (PDFs) is measured using the Fedorov table or using the EBSD mapping method. The presence of planar microstrutures is determined using BSE images and transmission electron microscopy. Planar microstrutures are observed for many minerals, most often for quartz (Fig. 1), feldspars, and are described in impactites and products of nuclear explosions. PDFs structures are a diagnostic feature of impacts and are used in this way to determine the genesis of deeply eroded structures. There are decorated differences among the planar elements. In which liquid inclusions contain droplets of melt or gas inclusions (Fig. 2). In zircon, planar microstrutures in natural impactites are rarely described and mainly studied based on experimental results.

Planar microstructures in zircons have been described in four large impact structures (Manicouagan, Rochechouart, Sudbury, Vredefort) preserved at different levels of the Earth's crust. (Garde et al. 2023). In the Manicouagan structure, planar deformations (PDFS) contain a large number of tiny pores with a diameter of less than 50 nm. They are decorated planar microstructures identical to such planar microstructures in quartz that form as a result of impact loads.

Planar microstructures (PDFs) for zircon have been described in experiments on impact metamorphism in the range of impact pressures 20-80 Gpa (Wittmann et. al., 2006). We have obtained new data on planar microstructures in zircon from natural impacts. They are observed in a wide range of impact transformations of zircon: in grains containing and not containing reidite (a high-density modification of zircon), as well as in grains with granular edges. Planar elements are observed in grains with partial decomposition of zircon into ZrO_2 and SiO_2, which occurs at temperatures above 1673°C, and in grains with a rim of melted glass like zircon, in diplect glass like zircon. They are observed

in a wide range of impact transformations of zircon: in grains containing and not containing reidite (a high-density modification of zircon), as well as in grains with granular rims. Reidite, a zircon polymorph with a scheelite structure formed under high pressure, was found fused with zircon in the samples subjected to impact. During the transition to reidite, the syngony of zircon remains, but the density of the structure increases.

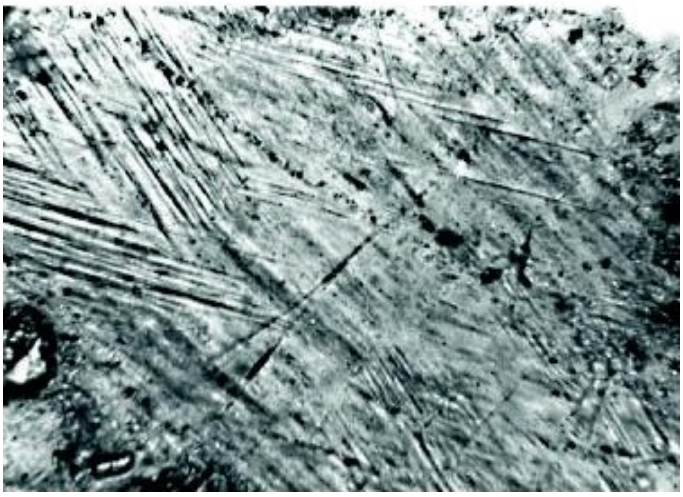

Fig.1.

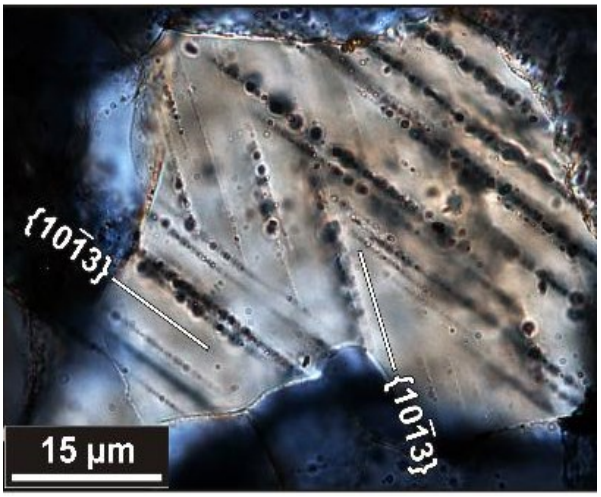

Fig.2.

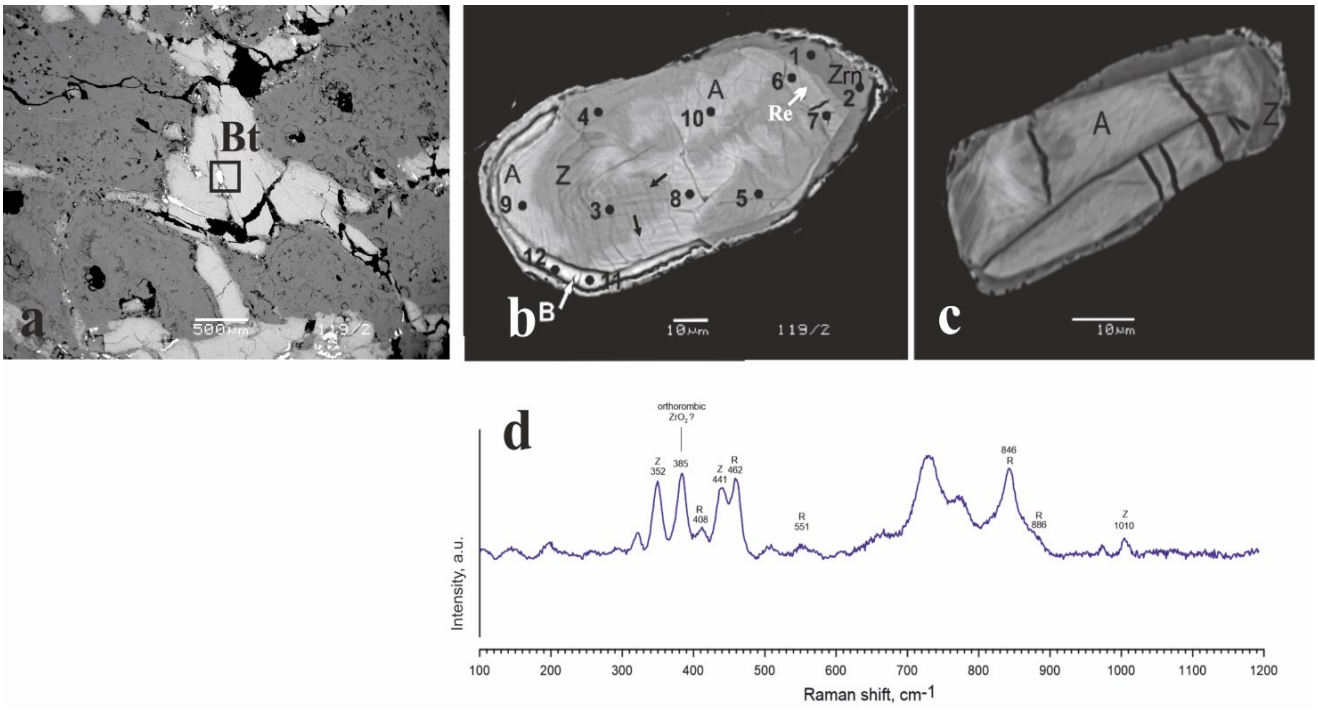

Fig.3.

Fig. 1. Planar microstructures in quartz (5 directions) from the Vorotilov borehole (Puchezh Katunskaya astrobleme), nichols are crossed, the diameter of the image is 4.5 mm.

Fig. 2. Decorated planar microstructures in quartz (junction of two individuals). The impact structure of Houghton (Canada**).**

Fig. 3 a,b - planar microstructures (PDFs) in a zircon grain located in a biotite crack. The Logoisk impact structure (Belarus). The directions of the planar microstructures are shown by arrows (Fig. 3-b). The grain contains reidite (Re), which has been proven by Raman spectroscopy. Zircon grain (Fig. B) it contains light areas due to the fine spraying of ZrO_2, proven by analyses.. the rim (shown in B) is represented by ZrO_2. Zircon grain with planar microstructures and absence of reidite. (Fig. c) (Fig. d) is the Raman spectrum of reidite, shown on (Fig. b).

According to experimental data, the presence of planar microstructures in grains with the absence of reidite is observed in the pressure range of 20 - 40 GPa, the complete transformation into reidite occurs at a pressure of 60 Gpa.

The presence of glass in zircon was confirmed by microraman spectroscopy. The redistribution of trace elements between zircon, diaplect glass according to zircon and metted glass according to zircon is considered.

In the Logoisk impact structure, planar microstructures in zircon occur in grains with partial decomposition of zircon to form ZrO_2 finely atomized in grains (Fig. 3b, c) and SiO_2 occurring at temperatures above 1673°C (Cavosie, Timms, Erickson, et al., 2018). At the same time, sections of zircon grains with planar elements without decay zones are preserved. Planar microstructures are observed in zircon with granular rims containing rounded ZrO_2 separations, which determines pressures of 65-70 GPa (Schmieder et al., 2015). Such a wide distribution of planar microstructures makes it possible to assess the conditions of their formation in each specific case.

The pressure at which planar microstructures are formed in zircon from suevite of a Logoisk impact structure can thus be estimated in the range of 40-70 GPa for grains containing and not containing reidite, as well as for grains with granular rims.

Conclusions

1. The formation of planar microstructures in zircon occurs at the solid-phase transformation of impact and refers to the diaplect transformations of minerals.
2. Taking into account the fixation of planar microstructures in zircon grains with varying degrees of impact transformation, it is possible to estimate the pressure at which planar microstructures are formed in zircon from suevite of a Logoisk structure, in the range of 40-70 GPa.

This study is fulfilled under to the state assignment of M.V. Lomonosov Moscow State University.

Acknowledgments *- We would like to thank the staff of the center for collective use "Electron probe microanalysis of mineral matter" (Faculty of Geology, Moscow State University, Department of Petrology and Volcanology) for assistance in research on the JSM-IT500 scanning electron microscope (Jeol, Japan) with the Oxford X-maxN energy dispersion spectrometer (Oxford Instrument Ltd., Great Britain). This equipment was purchased at the expense of the Moscow University Development Program.*

References:

Erickson et al., (2013). Experimental constraints on the onset of PFs, together with the absence of reidite, suggest a pressure range from 20 to 40 GPa

Erickson, T. M., Cavosie, A. J., Moser, D. E., Barker, I. R., and Radovan, H. A. (2013). Correlating Planar Microstructures in Shocked Zircon from the Vredefort Dome at Multiple Scales: Crystallographic Modeling, External and Internal Imaging, and EBSD Structural Analysis. American Mineralogist 98: 53–65.

Cavosie, A. J., and Folco, L. 2021. Shock-Twinned Zircon in Ejecta from the 45-m-Diameter Kamil Crater in Southern Egypt. In Large Meteorite Impacts and Planetary Evolution VI, edited by W. U. Reimold, and C. Koeberl, vol. 550, 419–430. Boulder, CO: Geological Society of America

Special Paper. https://doi.org/10.1130/2021.2550(17).

Cavosie, A. J., Timms, N. E., Erickson, T. M., and Koeberl, C. 2018. New Clues from Earth's most Elusive Impact Crater: Evidence of Reidite in Australasian Tektites from Thailand. Geology 46: 203–6.

Garde A.A, , Johansson L., N.Keulen N., .Schreiber A., Wirth R . Zircon Microstructures in Large, Deeply Eroded Impact Structures and Terrestrial Seismites. *Journal of Petrology*, 2023, 64, 1–23. https://doi.org/10.1093/petrology/egad079

Glazovskaya L.I., Shcherbakov V.D., Piryazev A.A. 2024**,** Logoisk impact structure, Belarus: Shock transformation of zircon, *Meteoritics and Planetary Science*, v. 59, № 1, p. 88-104.

Schmieder, M., Tohver, E., Jourdan, F., Denyszyn, S. W., and Haines, P. W. 2015. Zircons from the Acraman Impact Melt Rock (South Australia): Shock Metamorphism, U–Pb and 40Ar/39Ar Systematics, and Implications for the Isotopic Dating of Impact Events. Geochimica et Cosmochimica Acta 161: 71–100.

Wittmann, A., Kenkmann, T., and Schmitt, R. T. 2006. Shock-Metamorphosed Zircon in Terrestrial Impact Craters. Meteoritics & Planetary Science 41: 433–454.

Gorbachev P.N., Bezmen N.I. Modeling of the chondrite structure of carbonaceous meteorites at T=1000ºC, P=1 kbar in the presence of hydrogen. *UDC 550.4*

Korzhinskii Institute of Experimental Mineralogy RAS Chernogolovka, Chernogolovka, Moscow district, Russia
p_gor@mail.ru

Abstract. Chondrites are a type of stony meteorites characterized by the presence of chondrules – oval-shaped crystallized silicate precipitates in an Fe-sulfide-metal matrix. Carbonaceous chondrites, which make up the ultramafic group of chondrites rich in Mg, Ca and alkali metals, are of particular interest. The most controversial issue is the question of the conditions of chondrule formation. The experiments conducted continue the modeling of the chondrite structure using a high- gas-pressure vessel (HGPV) with hydrogen support at T = 1000ºC and a pressure of 1 K Bar using a model composition corresponding to carbonaceous chondrites.

Keywords*: chondrite, experiment, modeling, chondrules, matrix*

Experimental technique. The experiments were conducted in a high-pressure gas vessel (HGV) with internal heating. The starting composition was a model mixture similar in composition to the anhydrous meteorite Orgail. The mixture in the form of powder was pressed into a graphite capsule with a lid Ø 6 mm and a height of 15 mm. The capsule was placed in a Pt ampoule Ø 7 mm and a height of 60 mm, after which water and paraffin were added. The temperature of the experiments was 1000ºC, P = 1 kbar, $XH_2 = 0.3$, the duration was 24 hours. After the experiment, the graphite capsule was removed from the Pt ampoule and pressed. Fig. 1 shows the sample after the experiment. Then the sample was studied by optical methods and on a microprobe.

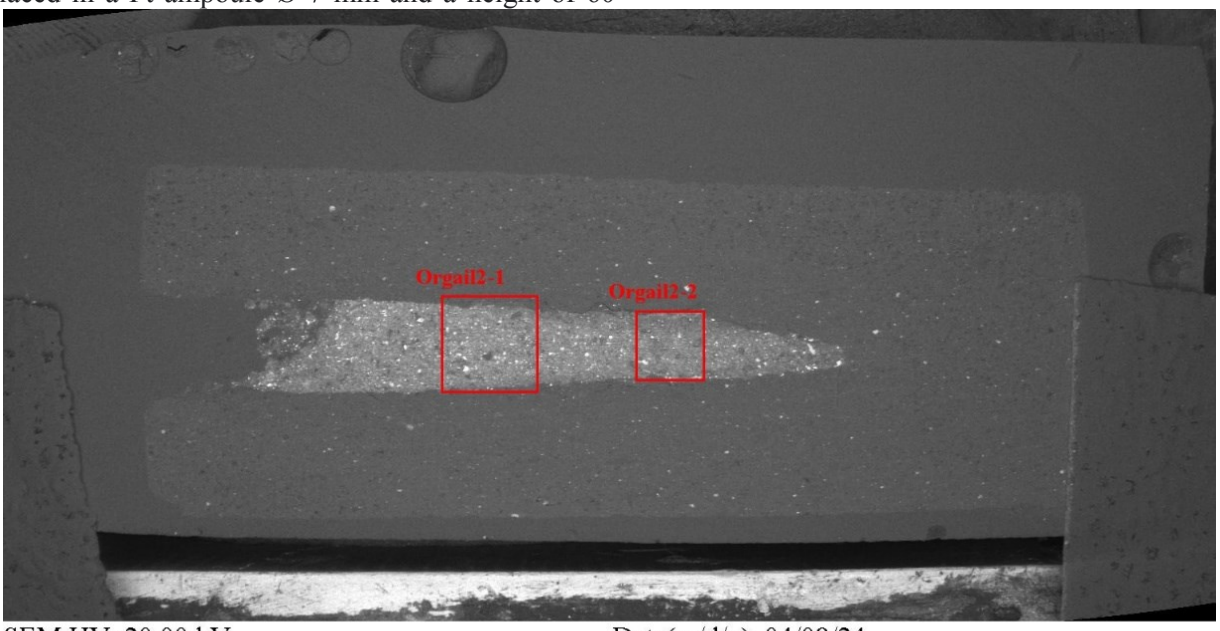

Fig. 1. Quenching sample after the experiment**.**

Results and discussion. The results of the experiment are presented in Table 1 and Fig. 2.

The quenched sample, the chemical composition of which is close to the composition of the original mixture, has a crystalline unevenly granular structure with rounded silicate inclusions, similar in chemical and phase composition to carbonaceous chondrites (Table 1, Fig. 2).

The matrix (analysis sites 10, 11) is characterized by a microgranular texture, ultra-basic composition, with a high content of magnesium (up to 34 wt.% MgO), iron (up to 19 wt.% FeO) with inclusions of silicate, Fe-metallic and Fe-sulfide phases.

The silicate fraction is represented by round and oval microinclusions (chondrules) from 10 to 40 μm in size, consisting of magnesian basalt, forsterite olivine and enstatite orthopyroxene. The ore fraction consists of intergrowths of metallic phases, almost pure Fe, Fe-Ni alloy with variable Fe and Ni content (from 3-6 to 16-22 wt.% Ni), and troilite.

Features of the texture, chemical and phase composition of the quenched samples indicate that recrystallization of the model starting mixture during the experiment led to the formation of carbonaceous chondrites.

Table 1. Comparison of the compositions (wt.%) of the Orgail carbonaceous chondrite with the general composition of the sample obtained during the experiment.

	Orgail	Exp.*	Matrix **	Chondrule ***
Na_2O	0.8	0.75	0.50	2.26
MgO	17.01	29.24	31.97	14.36
Al_2O_3	1.78	1.22	1.7	10.25
SiO_2	24.28	34.14	35.69	62.09
K_2O	0.08	0.11	0.14	0.54
CaO	1.31	1.24	1.13	6.22
H_2O	21.41		0.48	1.58
MnO	0.2	0.25	0.43	0.31
FeO	12.26	22.21	20.62	1.28
FeS	16.22			
NiO	1.32	1.22	0.63	0.06
C	3.34			
Total	100	100	100	100

Note : *Orgail carbonaceous chondrite (Voitkevich et al, 1990), * average composition of the quenched sample obtained in the experiment, ** average composition of the matrix of the quenched sample, *** average composition of oval-shaped microinclusions (chondrules)*

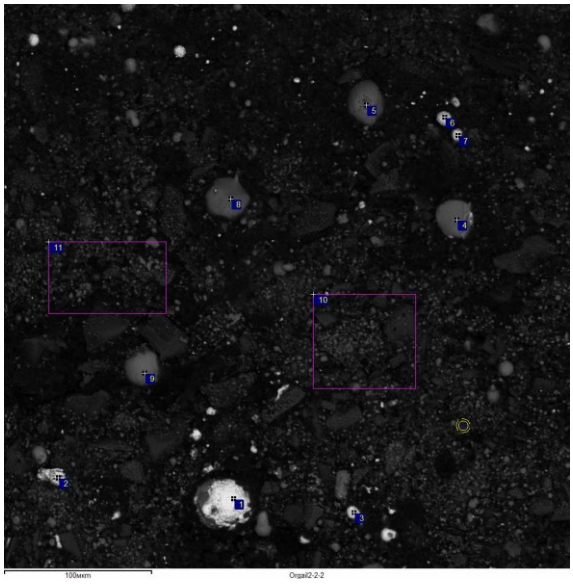

Fig. 2. Microphotograph of a section of a quenched sample with analyses.

This study is fulfilled under Research program № FMUF 2022-0004 of the Korzhinski Institute of Experimental Mineralogy.

Reference

Voitkevich G.V., Kokin A.V. and others. Handbook of geochemistry. - Moscow, Nedra. - 1990.

Guseva E.N. and Ivanov M.A. Spatial and genetic relationships of coronae - sources of young lobate fields and large volcanoes of Venus. *UDC 523.42*

Vernadsky institute of RAS, 119991, Moscow, Russia, guseva@geokhi.ru, ivanov.m@geokhi.ru

Abstract. We analyzed the regions of concentration of the coronae that represent the sources of young lobate plains and the large volcanoes of Venus and found that: (1) these features are genetically unrelated structures, spatially separated in many regions, but occur together in places; (2) the coronae are associated with regional extension zones, the volcanoes are associated with these zones to a lesser extent; (3) dome-like coronae are concentrated in rift zones, mainly in two regions: Ulfrun and Parga; (4) volcanoes are more widespread than the dome-like coronae. About half of the volcanoes are concentrated in three regions: Ulfrun, Parga, and Eistla and are not associated with extension zones. These regions likely mark the areas of localization of young volcanism on Venus.

Keywords: Venus, topography, coronae, volcanoes, young lavas, lobate plains, rift zones, groove belts, rifting and late volcanism.

Coronae are large concentric topographic features with the diameter up to 2500 km (Stofan et al., 1992; Crumpler, Aubele, 2000). Their annulus (topographic ridge) consists of closely spaced grooves and/or ridges (Barsukov et al., 1986; Nikishin, 1990; Pronin, Stofan, 1990). As a rule, materials of the plains surrounding the coronae (Stofan et al., 1992) embay the annulus. In most cases, corona volcanism occurs within their annulus. The formation of coronae is thought to be the result of ascending mantle diapirs (Nikishin, 1990; Pronin, Stofan, 1990; Smrekar, Stofan, 1997).

Previously, we established that three topographic classes characterize coronae: (1) class D, domed uplifts of the progressive stage of evolution of the parent diapir; (2) class W, complex depressions with a central peak corresponding to the stage when the domed uplift subsides without thermal support of the diapir; (3) class U, simple depressions of the end of the regressive stage (Guseva, Ivanov, 2022). Coronae were probably formed mainly in the Guinevrian and partly in the Atlian periods of the geological history of Venus (Basilevsky, Head, 1995; 2000; Ivanov, Head, 2011). Typical spatial associations of coronae indicate a probable genetic connection of coronae with regional extension zones (Stofan et al., 1997; Ivanov, Head, 2015).

Volcanic activity of most coronae died out mainly in the pre-Atlian period (Basilevsky, Head, 1995; 2000; Ivanov, Head, 2011). Only a small proportion of coronae (about 17% of the entire population) exhibit volcanism in the form of lobate plains (Guseva, Ivanov, 2023). Since the Atlian-age coronae are in most cases sources of lobate plains, the question arises as to how they are spatially and/or genetically related to volcanoes with their massive eruptions of Atlian lobate plains?

Most of the large volcanoes were formed in the late Atlian period (Head et al., 1992; Crumpler et al., 1997; Ivanov, Head, 2011, 2025). Their slopes are covered by numerous lava flows, which form complexes of young lobate plains (Head et al., 1992; Basilevsky, Head, 2007; Ivanov, Head, 2013; Hahn, Byrne, 2023). Lobate plains are sometimes intersected by fractures/grabens of rift zones, and sometimes embay them, which indicates their broadly synchronous formation (Ivanov, Head, 2013).

The goal of the study was to determine how the coronae sourcing lobate plains are related to the large volcanoes in terms of their spatial and size distribution. For that, we studied the morphological and topographic features of the coronae-sources of lobate plains (90 coronae) and the large volcanoes (88 structures) of Venus.

The coronae annulus is formed by either young rift structures, or older groove belt structures, or both. The most common sources of young lava flows are either extensional structures on the corona annulus or swarms of graben radiating from the

corona center. Less frequently, the source of the eruption is located inside the corona without morphological expression. Among the coronae-sources, the most common are domed coronae of class D (Fig. 1a), 40 out of 90 coronae (about 44% of the entire population). Their interior is elevated and is at a higher topographic level than the surrounding terrain outside the corona ridge. These coronae characterize the progressive stage of growth of a dome-shaped structure, when the parent diapir still has sufficient positive buoyancy to displace the lithospheric barrier upwards (Smrekar, Stofan, 1997). Less frequently, the coronae-source are of class W (Fig. 1b) or U (Fig. 1c), both include 25 coronae (28%). According to the model results (Smrekar, Stofan, 1997), the presence of a depression in the inner part of the corona indicates regressive stages of their evolution, when the parent diapir lost positive buoyancy due to cooling.

We used a new catalog of large volcanoes (Ivanov, Head, 2025), compiled after a thorough revision of the original catalog (Crumpler, Aubele, 2000), to study the spatial and genetic relationships of the volcanoes and coronae-sources of young lavas.

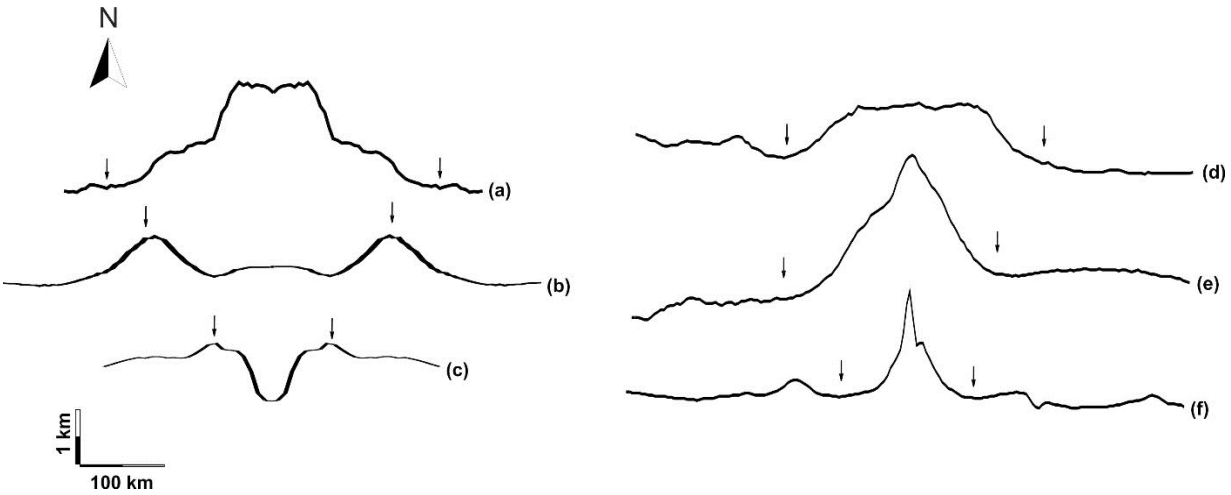

Figure 1 (a-f). Topographic profiles of coronae (left) and volcanoes (right): a – Nahas-tsan Mons corona, class D; b – Ereshkigal corona, class W; c – Rind corona, class U: d – Kokyanwuti Mons volcano, group 1; e – Idunn Mons volcano, group 2; f – Xochiquetzal Mons volcano, group 3. Arrows indicate an annulus of the coronae and a base of the volcanoes.

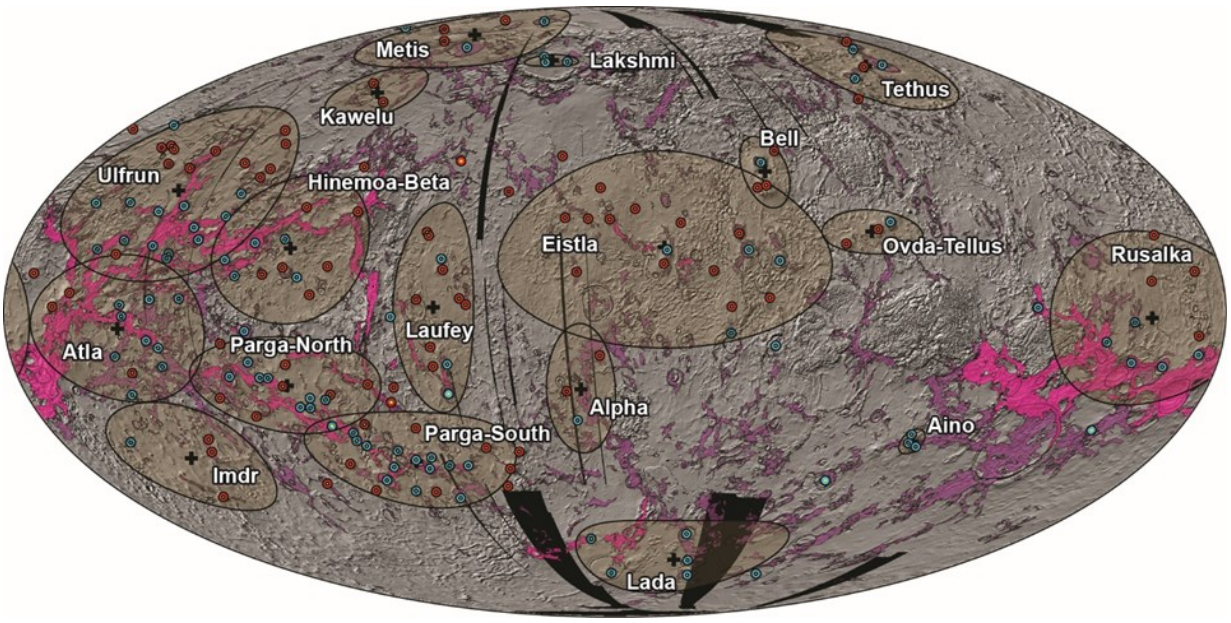

Figure 2. Regions of Venus where the large volcanoes and coronae-sources are predominantly concentrated. Volcanoes are shown in red, coronae in blue. Violet zones are groove belts, pink zones are rifts. The base is the surface topography obtained by the Hillshade method. The map is in the Mollweide equal-area projection. Geological boundaries by Global geological map of Venus (Ivanov, Head, 2011).

The large volcanoes are characterized by three size groups (Ivanov, Head, 2025): (1) the largest with an average diameter of 520 km and a flattened summit (Fig. 1d); (2) medium-sized conical, with the average diameter of 280 km and small summit region, where a piston-type caldera is often located (Fig. 1e); (3) small conical with the noticeably smaller average diameter of 140 km; they often lack the summit caldera (Fig. 1f). The most common on the surface of Venus are small conical volcanoes (about 48% of the entire population). Less common are flattened volcanoes with a flat top (26%) and medium conical volcanoes (26%).

We analyzed the concentration regions of the corona-sources and the large volcanoes using statistical methods (Principal component analysis and Discriminant function) and found that they are spatially separated in many regions, but in some regions they occur together (Fig. 2). We identified 18 regions of their concentration and analyzed the spatial and genetic relationships of the studied structures. The coronae-sources and the large volcanoes are genetically unrelated structures. They are spatially separated in many regions, such as the Metis, Ulfrun, Rusalka, Atla, Imdr, and Alpha regions (Fig. 2). In some regions, however, they occur together: Tethus, Hinemoa-Beta, Laufey, Eistla, Bell, Ovda-Tellus, Parga-N, and S. In some regions, such as Lakshmi, Aino, and Lada, lobate plains are source only by coronae, while in the Kawelu region only volcanoes represent the source of lobate plains. In all the regions, coronae are associated with regional extension zones such groove belts (e.g., Tethus) and/or rift zones (e.g., Ulfrun). Volcanoes are associated with these zones much less frequently (e.g., Eistla).

The main part (63%, 25 of 40 coronae) of the entire population of the domed coronae-sources is concentrated within the Ulfrun and Parga regions. The domed coronae are localized in these regions in fracturing zones that may have been reactivated in the late Atlian period of the geological history of Venus. About half (52%, 46 of 88 volcanoes) of the entire population of the large volcanoes are also localized in Ulfrun and Parga regions, as well as in the Eistla region.

Based on the obtained results, we can draw the following conclusions: (1) the coronae-sources and the large volcanoes are genetically unrelated structures, spatially separated in many regions, but co-occur in some regions; (2) the coronae-sources are associated with regional extension zones, volcanoes are associated with these zones to a lesser degree; (3) the dome-like coronae are concentrated in rift zones, mainly in two regions: Ulfrun and Parga; (4) volcanoes are more widespread than the dome-like coronae. About half of the volcanoes are concentrated in three regions: Ulfrun, Parga, and Eistla and are not associated with extension zones. These regions likely mark the areas of localization of young volcanism on Venus.

The study was carried out within the state assignment of the Vernadsky Institute of Geochemistry and Analytical Chemistry of the Russian Academy of Sciences (GEOKHI RAS).

References

1 Guseva E. N., Ivanov M.A. Coronae of Venus: geological, topographic and morphometric characteristics. Sol. Syst. Res. 2022. V. 56 (2). 76-83.

2 Guseva E.N., Ivanov M.A. Spatial and genetic relationships of coronae, lobate plains and rift zones of Venus. Sol. Syst. Res. 2023. V. 57 (2). 112-121.

3 Barsukov V.L., Basilevsky A.T., Burba G.A., Bobinna N.N., Kryuchkov V.P., Kuzmin R.O., Nikolaeva O.V., Pronin A.A., Ronca L.B., Chernaya I.M., and 20 co-authors. The geology and geomorphology of the Venus surface as revealed by radar images obtained by Venera 15 and 16. JGR. 1986. V.91. № B4. D378-D398.

4 Basilevsky A.T., Head J.W. Global stratigraphy of Venus: Analysis of a random sample of thirty-six test areas. EMP. 1995. V.66. 285-336.

5 Basilevsky A.T., Head J.W. Geologic units on Venus: Evidence for their global correlation. PSS. 2000. V.48. 75-111.

6 Basilevsky A.T., Head J.W. Beta Regio, Venus: Evidence for uplift, rifting, and volcanism due to a mantle plume. ICR. 2007. V.192. 167-186.

7 Crumpler L.S., Aubele J.C., Senske D.A., Keddie S.T., Magee K.P., Head J.W. Volcanoes and centers of volcanism on Venus. In Bougher S.W., Hunten D. M., Philips R. J. (Eds.), Venus II: Geology, geophysics, atmosphere, and solar wind environment. The Univ. of Arizona Press. 1997. 697-756.

8 Crumpler L.S., Aubele J. Volcanism on Venus, in Encyclopedia of Volcanoes, Houghton B., Rymer H., Stix J., McNutt S., Sigurdson H., Eds., San Diego: Acad. Press. 2000. 727-770.

9 Hahn R.M., Byrne P.K. A Morphological and Spatial Analysis of Volcanoes on Venus. JGR. 2023. 128. e2023JE007753.

10 Head J.W., Crumpler L.S., Aubele J.C., Guest J., Saunders R.S. Venus volcanism: Classification of volcanic features and structures, associations, and global distribution from Magellan data. JGR. 1992. V.97. 13.153-13.197.

11 Ivanov M.A., Head J.W. Global geological map of Venus. PSS. 2011. V.59. 1559-1600.

12 Ivanov M.A., Head J.W. The history of volcanism on Venus. PSS. 2013. V.84. 66-92.

13 Ivanov M.A., Head J.W. The history of tectonism on Venus: A stratigraphic analysis // PSS. 2015. 113-114. 10-32.

14 Ivanov M.A., Head J.W. Large volcanoes on Venus: Morphology, morphometry, and stratigraphy. ICR. 2025. V.429. 116404.

15 Nikishin A.M. Tectonics of Venus: A review, EMP. 1990. V.50/51. 101-125.
16 Pronin A.A., Stofan E. Coronae on Venus: Morphology and distribution. ICR. 1990. V. 87. 452-474.
17 Smrekar S.E., Stofan E.R. Corona formation and heat loss on Venus by coupled upwelling and delamination. SCI. 1997. V.277. 1289-1294.
18 Stofan E.R., Hamilton V.E., Janes D.M., Smrekar S.E. Coronae on Venus: morphology and origin//in: Bougher S.W., Hunten D.M., Phillips R.J. (Eds.). Venus II Geology, Geophysics, Atmosphere, and Solar Wind Environment. Univ. of Arizona Press. Tucson. 1997. 931-965.
19 Stofan E.R., Sharpton V.L., Schubert G., Baer G., Bindschadler D.L., Janes D.M., Squyres S.W. Global distribution and characteristics of coronae and related features on Venus: Implications for origin and relation to mantle processes. JGR. 1992. V.97 (E8). 13.347-13.378.

Guseva E.N. and Ivanov M.A. Comparison of rifting and volcanic activity of Atla and Beta Regiones, Venus. *UDC 523.42*

Vernadsky institute of RAS, 119991, Moscow, Russia, guseva@geokhi.ru, ivanov.m@geokhi.ru

Abstract. We assessed the scales of rifting and volcanism in Atla and Beta Regiones within a 2-km elevation contour and found that: (1) rifting is approximately 2 times and volcanism is approximately 4.5 times more widespread in Atla than in Beta; (2) young volcanic material in the study areas is mainly associated with large volcanoes; (3) several coronae are present in Atla, while they are absent in Beta. Such significant differences in the scale of rifting and volcanism probably reflect different lithospheric properties within Atla and Beta Regiones. Beta is characterized by abundant tesserae that are absent in Atla. It is likely that the tessera terrain in Beta may have served as a rheological/density filter for upwelling mantle flows, reducing the lithospheric permeability for them.

***Keywords**: Venus, topography, rift zones, volcanoes, lobate plains, coronae, rifting, volcanic activity.*

Atla and Beta Regiones are large topographic domes that are located in the western and northern parts of the BAT (Beta-Atla-Themis) region (Campbell et al., 1984; Stofan et al., 1995; Basilevsky and Head, 2007). They characterized by large gravimetric anomalies up to 200-300 mGl (Konopliv, Sjogren, 1994; Sjogren et al., 1997; Konopliv et al., 1999), the development of power zones of extension, and concentrations of younger (Atlian) volcanic activity in the form of lobate plains (Masursky et al., 1980; Shaber, 1982; Head et al., 1992; Basilevsky, Head, 2000; Ivanov, Head, 2011; 2013). The combination of these characteristics of studied regions interpreted as the result of rising mantle flows (McGill et al., 1981; Campbell et al., 1984; Kiefer, Hager, 1991; Stofan et al., 1995; Smrekar et al., 1997; Vezolainen et al., 2004; Davaille et al., 2017).

Rift zones start at the summits of the domes of Atla and Beta and extend as long (thousands of km) and wide (hundreds of km) belts of fractures and graben that in places are accompanied by abundant volcanism (Masursky et al., 1980; Schaber, 1982; Campbell et al., 1984; Head et al., 1992; Ivanov, Head, 2015; Guseva, 2016). Volcanism typically occurs as extensive lobate plains, the fields of which can be hundreds of kilometers across and often extend from large volcanoes, but sometimes have no discernible source (Head et al., 1992; Crumpler et al., 1997; Smrekar et al., 1997; Ivanov, Head, 2011; 2013; 2015).

The goal of our study was to estimate the scale of rifting and volcanism in Atla and Beta by estimation of the total areas of rift zones and lobate plains spatially associated with different type of sources. The Atla and Beta Regiones belong to the highland topographic domain (Masursky et al., 1980), and their boundary is defined by the 2 km elevation contour. Areas of the domes within this contour line is ~ 3.17 x 10^6 km^2 for Atla and ~ 3.26 x 10^6 km^2 for Beta. Areas of rifts and fields of lobate plains were taken from the global geological map (Ivanov, Head, 2011).

Dome of Atla Regio is about 1200-1600 km across and approximately 2.5 km high (Phillips and Malin, 1984; Senske et al., 1992). Dome of Beta Regio is larger and higher than dome of Atla Regio and is about 2000 km across, extends meridionally for 2500 km, and reaches a height of about 4-5 km (McGill et al., 1981; Campbell et al., 1984; Stofan and Smrekar, 1995; Smrekar et al., 1997; Basilevsky and Head, 2007). These differences in the topographic features of the studied domes explained by the fact that they formed in different geological environments: large massifs of tessera are widespread in the Beta region, while only isolated tessera fragments are found in the Atla region (Ivanov, Head, 1996). Probably, the uplift in Atla began within the midlands presented by shield and regional plains (the altitude 0-2 km, Masursky et al., 1980), and in the Beta – in the highlands (above the altitude level of 2 km, Masursky et al., 1980) composed mainly by the tessera terrain (Senske et al., 1992).

Domes of the Atla and the Beta are characterized as rifts bearing, with rift zones extending from their summits. In the Atla region, rifting is more extensive than in the Beta region. We estimated the total area of the rift zones as ~ 1.89 x 10^6 km^2 for the Atla (Fig. 1a) and ~ 0.83 x 10^6 km^2 for the Beta (Fig. 1b). Common topographic features characterize the rift zones in both regions. In the area of origin (on the domes) and attenuation, these are simple V-shaped depressions and in the middle part rifts are complex

W-shaped depressions with a central heights.

Lava plains are spatially associated with rift zones of Atla and Beta (Head et al., 1992; Stofan, Smrekar, 1995; Smrekar et al., 1997; Ivanov, Head, 2015). Lava plains are characterized as stratigraphically young complexes (unit pl) in Atla and Beta. In the studied regions, they are associated with large volcanoes, rifts, and sometimes with coronae (Fig. 1). We estimated the total area of lobate plains in Atla to be approximately 1.75 x 10^6 km². All flows of lobate plains are represented by material erupted from the large volcanoes Ozza and Maat Mons (d ~ 576 and 427 km, h ~ 2.2 and 6.1 km, respectively, Ivanov, Head, 2025). The total area of lobate plains in Beta is approximately 0.38 x 10^6 km²; this material was erupted from the large volcano Theia Mons (d ~ 520 km, h ~ 1.7 km, Ivanov, Head, 2025).

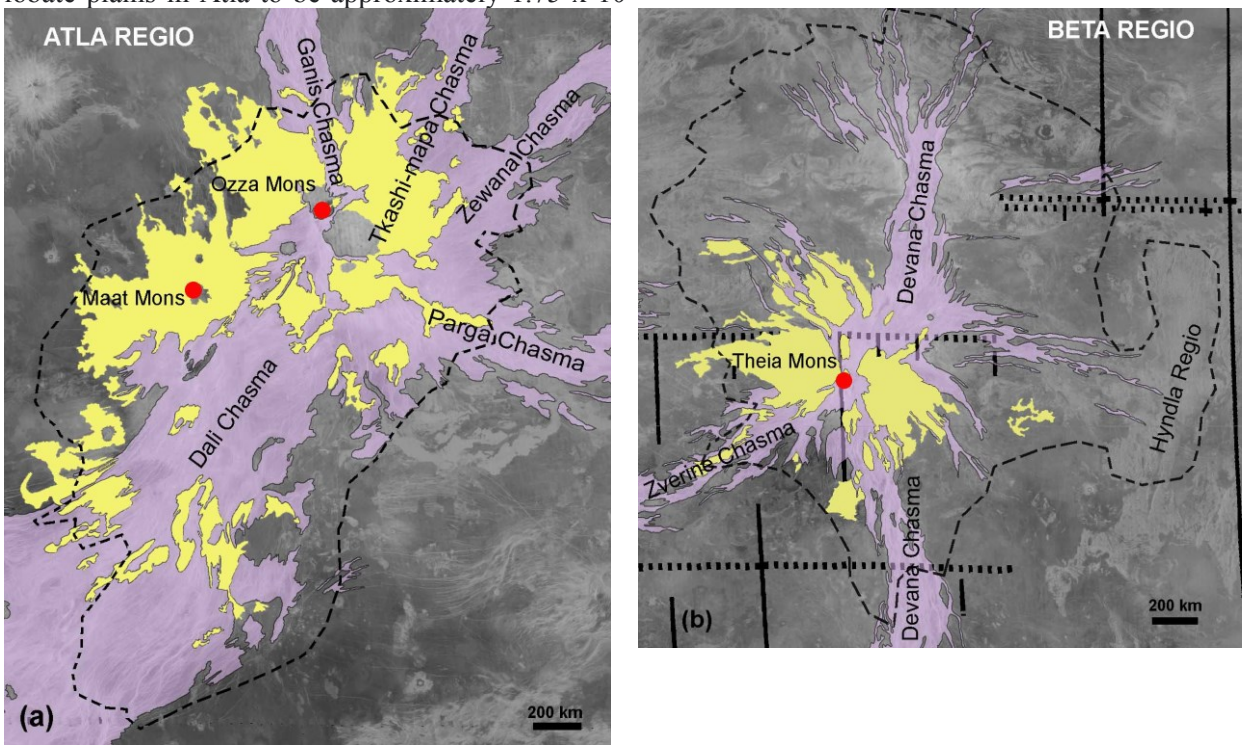

Figure 1. Atla (a) and Beta (b) Regiones; lobate plains - yellow and rift zones - purple; red dots are large volcanoes; black dotted line are contour of 2 km. Geological boundaries according to (Ivanov, Head, 2011).

In addition, Atla Regio is characterized by the presence of several coronae, mainly of the domed topographic class, while such structures are absent in the Beta Regio (Guseva, Ivanov, 2020).

The results of our study can be summarized as follows: (1) rifting is approximately 2 times and volcanism is approximately 4.5 times more widespread in Atla than in Beta; (2) young volcanic material in the study areas is mainly associated with large volcanoes; (3) several coronae are present in Atla, while they are absent in Beta. Such significant differences in the scale of rifting and volcanism probably reflect different lithospheric properties within Atla and Beta Regiones. Beta is characterized by abundant tesserae that are practically absent in Atla. It is likely that the tessera terrain in Beta region may have represented a rheological/density filter for upwelling mantle flows, reducing the lithospheric permeability for them.

The work was carried out within the state assignment of the Vernadsky Institute of Geochemistry and Analytical Chemistry of the Russian Academy of Sciences (GEOKHI RAS).

References

1 Basilevsky A.T., Head J.W. Rifts and large volcanoes on Venus: Global assessment of their age relations with regional plains /// JGR. 2000. 105. 24583-24611.

2 Basilevsky A.T., Head J.W. Beta Regio, Venus: Evidence for uplift, rifting, and volcanism due to a mantle plume // ICR. 2007. 192. 167-186.

3 Campbell D.B., Head J.W., Harmon J.K., Hine A.A. Venus volcanism and rift formation in Beta Regio // SCI. 1984. 226. 167-170.

4 Crumpler, L.S., Aubele, J.C., Senske, D.A., Keddie, S.T., Magee, K.P., and Head, J.W., Volcanoes and centers of volcanism on Venus // Venus II / Eds Bougher S., Hunten D., Phillips R. Univ. Arizona Press. 1997. 697-756.

5 Davaille A., Smrekar S.E., Tomlinson S. Experimental and observational evidence for plume-induced subduction on Venus // Nature Geoscience. 2017. V. 10(5). 349-355.
6 Guseva E.N. Classification of the Rift Zones of Venus: Rift Valleys and Graben Belts // SSR. 2016. 50 (3). 184-196.
7 Guseva E. N., Ivanov M.A. Structures of Coronae on Venus: Results of Topographic and Geologic Analysis // SSR. 2020. V. 54. № 6. 497-503
8 Head J.W., Crumpler L.S., Aubele J.C., Guest J., Saunders R.S. Venus volcanism: Classification of volcanic features and structures, associations, and global distribution from Magellan data // JGR. 1992. 97. 13.153-13.197.
9 Ivanov M., Head J. Tessera terrain on Venus: A survey of the global distribution, characteristics, and relation to surrounding units from Magellan data // JGR. 1996. 101 (E6). 14861-14908.
10 Ivanov M.A., Head J.W. Global geological map of Venus // PSS. 2011. 59. 1559-1600.
11 Ivanov M.A., Head J.W. The history of volcanism on Venus // PSS. 2013. 84. 66-92.
12 Ivanov M.A., Head J.W. The history of tectonism on Venus: A stratigraphic analysis // PSS. 2015. 113-114. 10-32.
13 Ivanov M.A., Head J.W. Large volcanoes on Venus: Morphology, morphometry, and stratigraphy // ICR. 2025. V. 429. 116404.
14 Kiefer W., Hager B. A mantle plume model for the equatorial highlands of Venus // JGR. 1991. 96. 20497-20966.
15 Konopliv A.S., Banerdt W.B., Sjogren W.L. Venus Gravity: 180th degree and order model // ICR. 1999. 139. 3-18.
16 Konopliv A.S., Sjogren W.L. Venus spherical harmonic gravity model to degree and order 60 // ICR. 1994. V. 112. P. 42-54.
17 Masursky H., Eliason E., Ford P.G., McGill G.E., Pettengill G.H., Schaber G.G., Schubert G. Pioneer-Venus radar results: Geology from the images and altimetry // JGR. 1980. 85 (A13). 8232-8260.
18 McGill G.E., Steenstrup S.J., Barton C., Ford P.G. Continental rifting and the origin of Beta Regio, Venus // GRL. 1981. 8 (7). 737-740.
19 Phillips R.J., Malin M.C. Tectonics of Venus, Ann. Rev. // EPS. 1984. V. 12. P. 411-443.
20 Schaber G.G. Venus: limited extension and volcanism along zones of lithospheric weakness // GRL. 1982. V.9. 499-502.
21 Senske D.A., Schaber G.G., Stofan E.R. Regional topographic rises on Venus: Geology of western Eistla Regio and comparison to Atla Regio and Beta Regio//JGR. 1992. V.97. 3395-13420.
22 Sjogren W.L., Banerdt W.B., Chodas P.W., Konopliv A.S., Balmino G., Barriot J.P., Arkani-Hamed J., Colvin T.R., Davies M.E. The Venus Gravity Field and Other Geodetic Parameters // Venus II / Eds Bougher S., Hunten D., Phillips R. Univ. Arizona Press. 1997. 1125-1161.
23 Smrekar S.E., Stofan E.R., Kiefer W.S. Large volcanic rises on Venus // Venus II / Eds Bougher S., Hunten D., Phillips R. Univ. Arizona Press. 1997. 845-878.
24 Stofan E.R., Smrekar S.E. Large topographic rises on Venus: Implications for mantle upwelling // JGR. 1995. 100. 23.317-23.327.
25 Vezolainen A.V., Solomatov V.S., Basilevsky A.T., Head J.W. Uplift of Beta Regio: Three-dimensional model // JGR. 2004. V. 109. 1-8.

Khisina N.R., Teplyakova S.N., Korochantsev A.V., Abdrakhimov A.M. Carbonaceous chondrite clast in the Elga iron meteorite. *UDC 552.61*

Vernadsky Institute RAS, Russia, 119334, Moscow, Kosygina 19, khisina@gmail.com

Abstract . The TEM, SEM and Raman spectroscopy study showed that a melt pocket in one of the silicate inclusions in the Elga iron meteorite is a clust of carbonaceous chondrite trapped by Elga's parent body in a collisional event.

Keywords: *iron meteorite Elga, carbonaceous chondrites, macromolecular carbon, siderite, sarcopside, liquid immiscibility in melts, TEM, EELS, Raman spectroscopy*

Introduction. A melt pocket (a region of localized shock-induced melting) identified in one of the silicate inclusions of the Elga iron meteorite (Fig. 1) was investigated using transmission electron microscopy (TEM), scanning electron microscopy (SEM), and Raman spectroscopy (Khisina et al., 2017; Khisina et al., 2019). The melt pocket (Fig. 1b) exhibits liquid immiscibility between a phosphide phase (schreibersite, $(FeNi)_3P$) and oxygen-bearing phases—siderite (region 1) and sarcopside (region 2). The results reveal an unusual composition of the melt pocket, whose mineralogy and bulk chemistry are inconsistent with those of the silicate inclusions in this meteorite. (1) The high content of oxidized Fe in the melt pocket contrasts with the low FeO concentration (~3 wt.%) in the SiO_2 glass of the silicate inclusions. (2) Only Fe and Si are present as cations in the melt pocket, with Fe being the dominant element. (3) Pure siderite and pure sarcopside - the main oxygen-bearing phases in the melt pocket - are not typically found in ordinary chondrites or iron meteorites. These variances lead to the conclusion that the melt pocket represents a remelted foreign fragment that was accreted by the Elga parent body during a collisional event. The presence of carbonaceous compounds identified in the melt pocket suggests that the accreted fragment belongs to the carbonaceous chondrite class.

Results. In region 1 of the melt pocket, siderite grains exhibit coarsening, a loss of globular morphology, and the development of sinuous grain boundaries in contact with schreibersite (Fig. 2). Narrow SiO_2-rich rims are commonly observed surrounding the siderite grains. These rims are typically discontinuous around larger siderite grains

(Fig. 2a) but appear closed around smaller, more rounded grains (Fig. 3). Within the SiO_2-bearing rims, fine inclusions of Ni-phosphide are present (Fig. 2a). Carbonaceous material was identified in both siderite and sarcopside, as confirmed by electron energy loss spectroscopy (EELS) (Fig. 2c) and Raman spectroscopy (Fig. 4b), respectively. In siderite, EELS spectra reveal carbon bonding structures consistent with phenolic and aryl ether groups (Fig. 2c). These findings are in agreement with the spectral characteristics of carbonaceous matter in phyllosilicates and clays of carbonaceous chondrites such as Orgueil, Ivuna, and Tagish Lake (Garvie et al., 2005; 2007). Raman spectra obtained from sarcopside indicate the presence of carbon in the sp^2-hybridized state, typical of aromatic hydrocarbons (Fig. 4b). In addition to the carbonaceous matter, clusters of fine Ni-phosphide inclusions are also observed within both siderite and sarcopside.

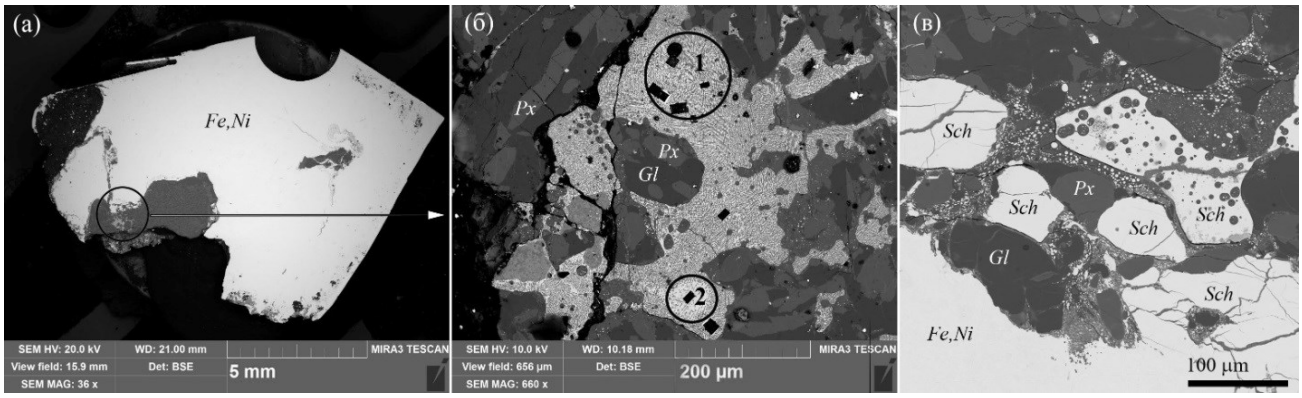

Figure. 1. Thin section photomicrographs of the melt pocket in the Elga iron meteorite. (a) Reflected light. A silicate inclusion (gray) embedded within the Fe,Ni metal matrix (also gray) contains a melt pocket (circled). (b) BSE image of the melt pocket. Circles indicate analyzed areas. Region 1 shows siderite–phosphide liquid immiscibility; Region 2 shows phosphate–phosphide liquid immiscibility. Black rectangles mark areas extracted for focused ion beam (FIB) sectioning. Px – pyroxene; Gl – silicate glass. (c) Brecciated portion of the silicate inclusion at the interface with Fe,Ni metal. This area contains fragments of a schreibersite rim (Sch), pyroxene, and silicate glass. Numerous Fe,Ni metal globules (bright white) are embedded in the silicate glass, indicating interaction and mixing of silicate melt with molten Fe,Ni metal.

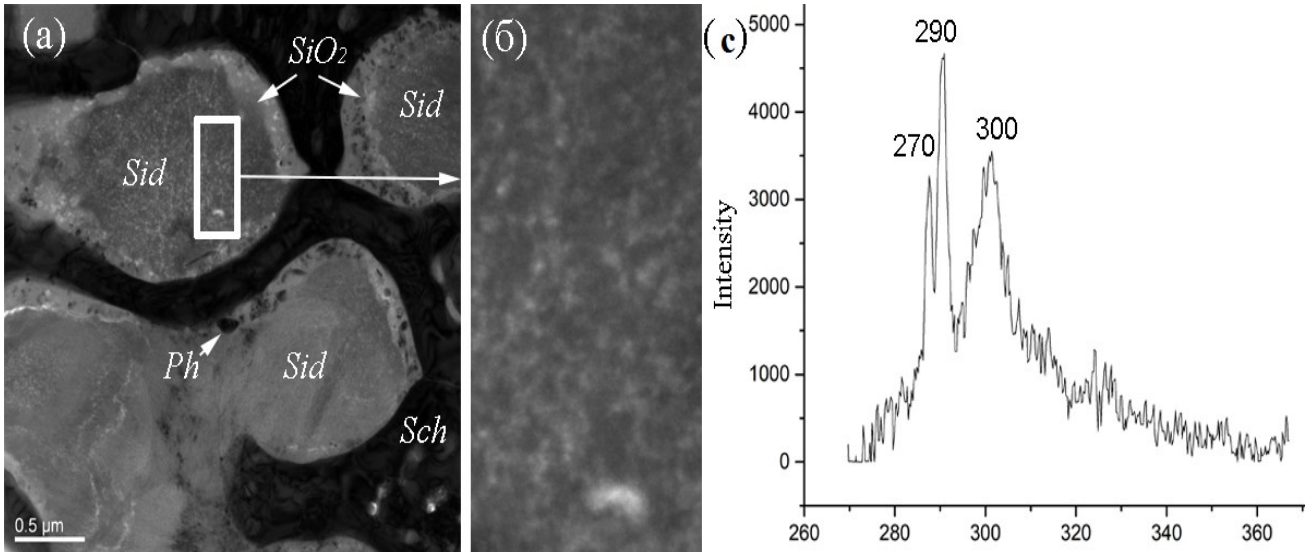

Figure. 2. Siderite–phosphide interaction at the nanoscale. (a) Siderite (Sid) inclusions within a schreibersite (Sch) matrix. A SiO_2-rich rim at the Sid–Sch interface contains Ni-phosphide inclusions (black) and fine carbonaceous particles (white dots). The siderite hosts dispersed light-contrast inclusions, interpreted as hydrocarbon phases (phenols and aryl ethers). HAADF image in TEM mode. (b) Magnified view of the boxed region in (a). (c) EELS spectrum of siderite. Peaks at 290 eV and 300 eV correspond to carbonate; the 270 eV peak is attributed to phenolic hydrocarbon groups.

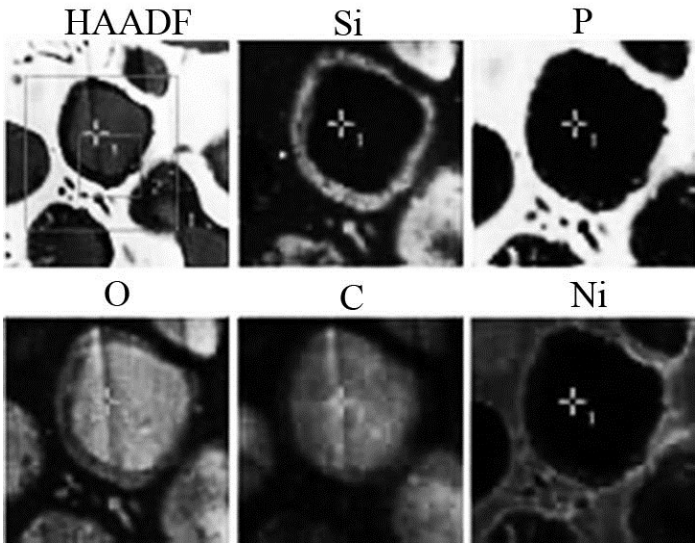

Figure. 3. Elemental mapping of a globular siderite grain, exhibiting a SiO_2-rich rim

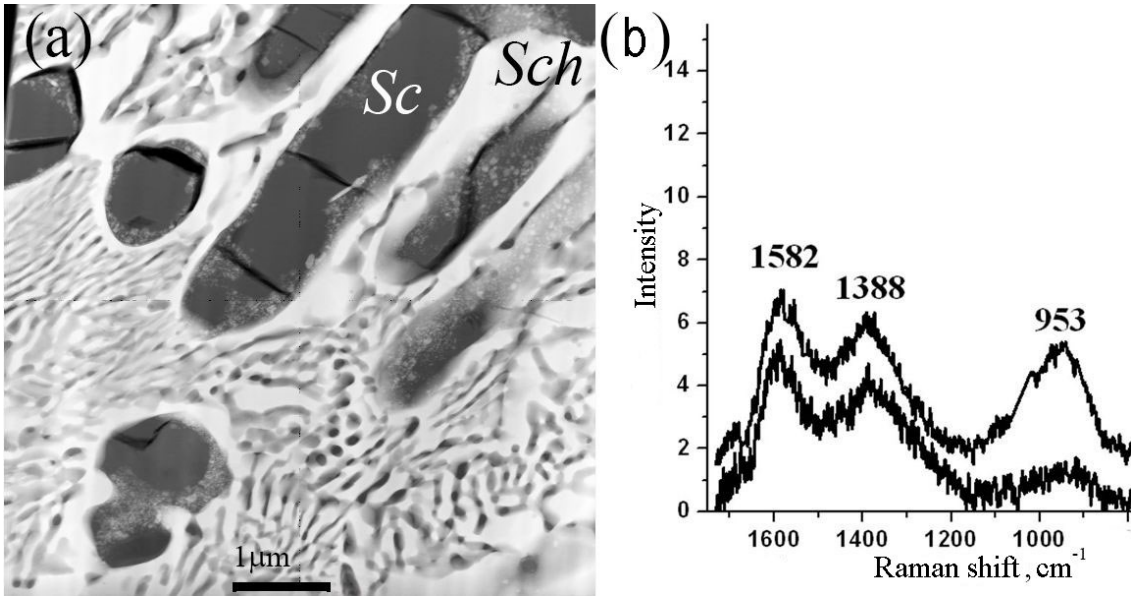

Figure. 4. Sarcopside and associated phases in Region 2 of the melt pocket. (a) HAADF/TEM image. Cluster of fine-grained Ni-phosphide inclusions within sarcopside (Sc). (b) Raman spectrum of sarcopside. Peaks at 1388 cm^{-1} and 1582 cm^{-1} are assigned to sp^2-hybridized carbon, while the peak at 953 cm^{-1} corresponds to sarcopside.

Conclusions. Dispersed carbonaceous matter is commonly observed in ordinary chondrites. Compact fragments (clasts) of carbonaceous chondrites have occasionally been identified within H chondrite material (Patzek et al., 2018; Kebukawa et al., 2017; Rubin et al., 2005). The origin of such clasts is typically attributed to impact events in space, where small carbonaceous chondrite bodies (impactors) collided with larger H chondrite parent target bodies. These collisions likely led to the fragmentation of the carbonaceous bodies and the incorporation of resulting fragments into the regolith of the H chondrite parent body.

In the case of the Elga meteorite, such an event may have occurred after differentiation of the parent body and the formation of a metallic core. The carbonaceous clast embedded within the silicate inclusion in Elga appears to have been composed of magnetite, carbonaceous compounds, and silicates. It is plausible that the mechanical integrity of this fragment was preserved due to the presence of magnetite. A subsequent catastrophic impact likely caused mixing of carbonaceous chondrite material with silicate matter and FeNi metal of the H chondrite in an ejecta plume.

The elevated temperatures recorded in the carbonaceous clast, relative to the surrounding silicate matrix in Elga, may be explained by the presence of volatile-rich gases and the inherently low shock resistance of carbonaceous material. As is well known, shock waves lose kinetic energy when propagating through such materials, with the energy being converted into heat.

Magnesium-calcium carbonates with minor Fe substitutions are frequently found in ordinary chondrites and are generally interpreted as products

of aqueous alteration on their parent bodies (i.e., hydrothermal processes). However, our results indicate that under specific conditions, carbonates may also form by crystallization from a hydrocarbon-bearing impact melt. This represents an alternative mechanism for carbonate formation in meteorites.

Acknowledgments. The authors are grateful to R. Wirth for assistance with TEM data acquisition and to A.A. Shiryaev for support in obtaining Raman spectra.

Funding: This work was carried out within the State Assignment of the V.I. Vernadsky Institute of Geochemistry and Analytical Chemistry, Russian Academy of Sciences.

References

1. Garvie L. A. J., Buseck P. R. Prebiotic carbon in clays from Orgueil and Ivuna (CI), and Tagish Lake (C2 ungrouped) meteorites // Meteorit. Planet. Sci. 2007. V. 42. No.12. P. 2111–2117.
2. Garvie L. A. J., Craven A. J. Structure and bonding of carbon in clays from CI carbonaceous chondrites // 36th Annual Lunar and Planetary Science Conference. 2005. P. 1515.
3. Kebukawa Y., Zolensky M. E., Chan Q. H. S., Nagao K., Kilcoyne A. L. D., Bodnar R. J., Cody G. D. (2017) Characterization of carbonaceous matter in xenolithic clasts from the Sharps (H3.4) meteorite: Constraints on the origin and thermal processing // Geochim. Cosmochim. Acta. 2017. V. 196. P. 74–101
4. Khisina N. R., Teplyakova S. N., Wirth R. et al. Carbon-bearing phases in shock-induced melt zones of the Elga meteorite // Geochem. Int. 2017. V. 55. P. 317–329.
5. Khisina N. R., Wirth R., Abdrakhimov A. M. Liquid Immiscibility in Regions of Localized Shock-Induced Melting in the Elga Meteorite // Geochemistry International. 2019. V. 57. No. 8. P. 903-911.
6. Patzek M., Bischoff A., Visser R., John T. Mineralogy of volatile-rich clasts in brecciated meteorites // Meteorit. Planet. Sci. 2018. V. 53. P. 2519-2540.
7. Rubin A. E., Trigo-Rodriguez J. M., Kunihiro T., Kallemeyn G. W., Wasson J. T. Carbon-rich chondritic clast PV1 from the Plainview H-chondrite regolith breccia: Formation from H3 chondrite material by possible cometary impact // Geochim. Cosmochim. Acta. 2005. V. 69. No. 13. P. 3419–3430.

Krasilnikov A.S., Ivanov M.A. Determination of the mixing factor of local and foreign material in the Langrenus crater ejecta.

Vernadsky Institute of Geochemistry and analytical Chemistry RAS, 119991, Moscow, Russia
krasilnikov_as@geokhi.ru

Abstract. Based on the data on the iron oxide content in the rays of the Langrenus crater, a relationship has been definite that describes the ratio of the Mare Fecunditatis regolith to the material of the crater ejecta. This ratio represents a mixing factor of local and foreign material formed during the fall of craters ejecta. The data obtained make it possible to refine the currently existing mixing models.

***Keywords**: The Moon, Langrenus, Mare Fecunditatis, rays, ejecta, mixing factor.*

Introduction. Determining the material mixing factor when impact crater ejecta are formed, is one of the main tasks, the solution of which will help to clarify our knowledge of the distribution of material on the Moon. Understanding the distribution of material provides information on the composition of certain ejecta, as well as their origin. However, the existing models of ejecta emplacement and their mixing differ greatly, and therefore the material mixing factor needs to be studied further.

Mixing factor of local and foreign materials. There are a series of models (McGetchin et al., 1973; Pike, 1974; Fassett et al., 2011; Housen et al., 1983; Sharpton, 2014) that give a representation of the thickness of ejecta deposits, however, do not take into account the inevitable mixing of ejecta material with the underlying regolith. During the emplacement of ejecta deposit, broad sizes materials fall out, forming secondary impact craters in a wide range of diameters. As the result, the regolith of the near-surface layers is mixed with the ejecta material. An approach to the solution of the mixing problem was proposed in work Oberbeck et al. (1975), where presented the results of studies to quantify evaluation of volume ratio of the local to the introduced material of ejecta (mixing factor μ). Oberbeck et al. (1975) conducted a series of experiments and studied secondary craters of some primary craters on the Moon and they managed to create empirical relation of the change in the value of μ as the distance from the crater increases:

$$\mu = 0.0183*R^{0,87} \quad (1),$$

where R – distance from the middle of the crater radius to the point of calculated its ejecta.

Oberbeck et al. (1975) brought arguments that this relationship can be applied not only to determine the degree of mixing of ejecta from the Copernicus crater, but also for other large lunar craters. The R value was chosen to be equal to the distance from the middle of the crater radius to the calculation site because it is not possible to determine from which part of the crater a fragment, which caused formation of a secondary crater, was ejected.

In their work, Petro and Pieters (2006) compared the results of various ejecta deposition models, including models with and without material mixing. The authors determined that the results obtained using the mixing model of Oberbeck et al. (1975) are

poorly comparable with the geochemical and petrographic features of the Apollo 16 soil (Korotev, 1997). This discrepancy led Petro and Pieters (2006) to the conclusion that the mixing factor μ calculated from formula (1) should be reduced about by a factor of two.

Estimation of the mixing of local and foreign materials by the data about content of iron oxide in the rays of the Langrenus crater

At the moment, there is no exact confirmation of the correctness of the material mixing models. In order to refine them, the models were compared with data on the content of iron oxide in the lunar regolith, estimated from the results of the Clementine mission (Lucey and Blewett, 2000).

The rays of the Langrenus crater (Fig. 1) were taken as the object of study, which was selected because:

(1) it is located on the border of the Mare Fecunditatis and the highlands, and part of its rays are clearly visible on the dark and smooth mare surface;

(2) the age of the crater, 3.44 Ga (Ivanov et al., 2023), almost coincides with the age of the mare surface of the Mare Fecunditatis, 3.37 Ga (Ivanov et al., 2023), which minimizes the difference in the regolith aging of the rays and the mare surface due to mechanical reworking of regolith by ejected particles.

In our study, were used only those rays that lie on the smooth surface of the mare. Within each of them, were have selected randomly distributed points, at which the model FeO content was determined. The obtained estimates of FeO content form a clearly defined trend of increasing iron oxide, as the distance (D) from the center of the crater increases (Fig. 2), which is described by a linear function:

$$FeO = 0{,}0000236*D + 9{,}62 \quad (2),$$

where D – distance from the crater center in meters, FeO – iron oxide content in wt%.

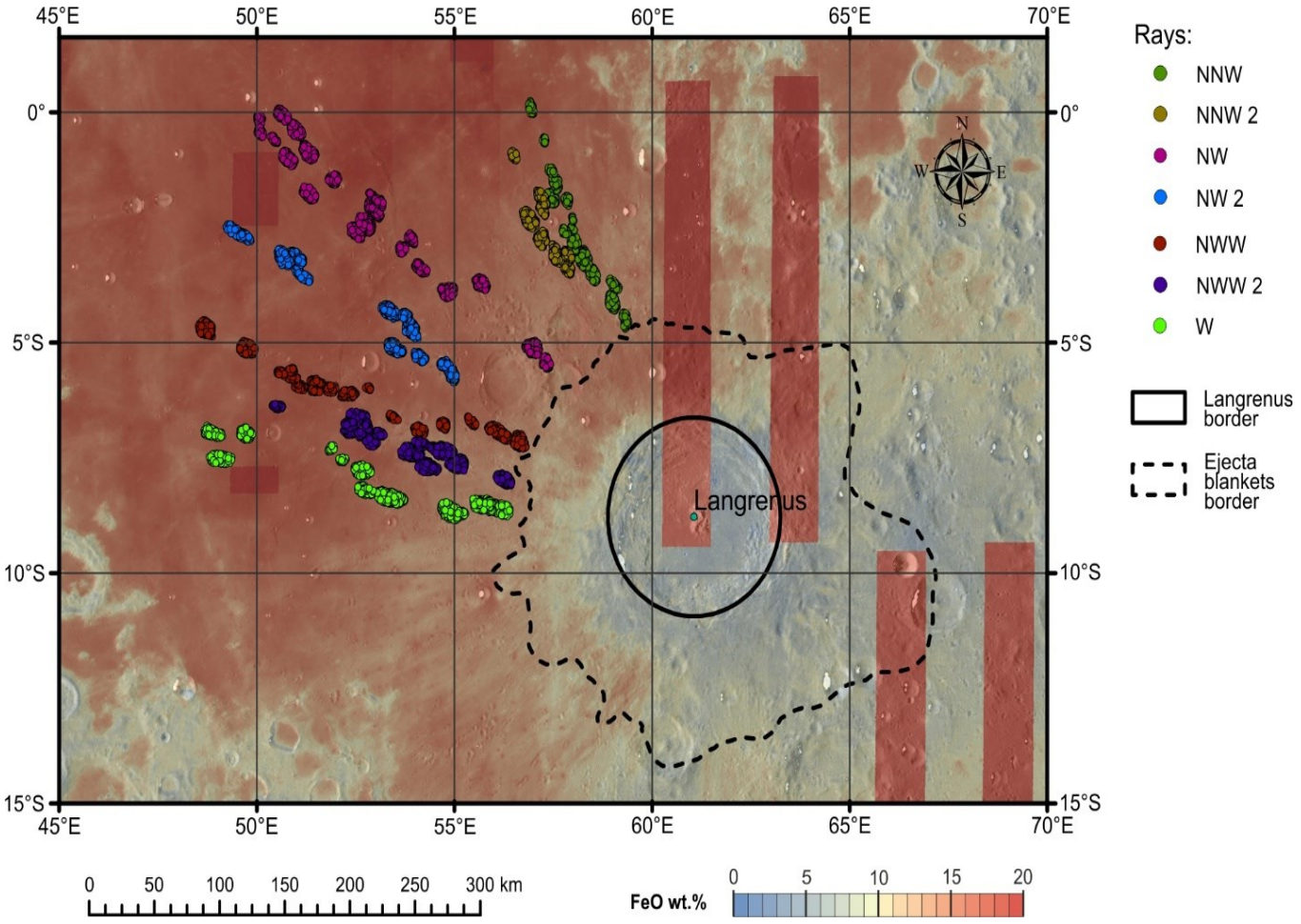

Fig. 1. Map of the FeO content in the area of the Langrenus crater and the rays used in the calculations.

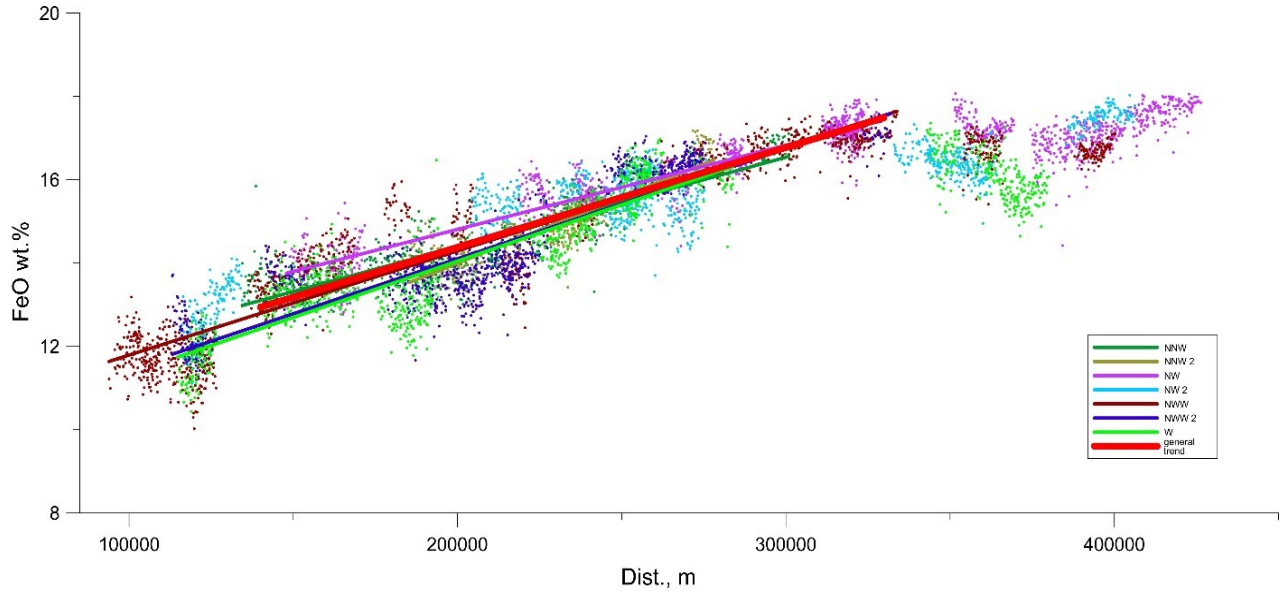

Fig. 2. Change in the amount of iron oxide in the rays of the Langrenus crater depending on the distance from its center.

At the distance of about 3 crater diameters (~300 km), the curve flattens out and no increase in iron content in the rays is observed, and the local variations in the FeO content are associated with the presence of rays from Tycho crater. We consider the increase in iron oxide as a result of the mixing of two end members: mare material with an average FeO content of 17.5 wt.%, and highland materials with an average FeO content of 5.5 wt.%. The determined function (2) shows that directly outside the zone of continuous ejecta at a distance of ~150 km from the center of the crater, the content of iron oxide is ~13.16 wt.%, which, at the indicated contents of iron oxide in the end-members, corresponds to a mix of ~ 36 and 64% of the highland and mare components. At a distance of 330 km, where the horizontal part of the trend begins, the iron oxide content is estimated to be ~17.5 wt.%, which practically coincides with the average FeO content in the Mare Fecunditatis regolith and, therefore, corresponds to almost 100% of the mare component.

The obtained dependence (2) allows us to propose a formula for estimating the proportion of foreign/local material (L/F) in the range of distances from the zone of contiguous ejecta (~100 km) to the one where the local regolith absolutely dominate (~300 km):

$$L/F = 0{,}2*\exp(0{,}013D) \quad (3),$$

where D – distance from the crater center in kilometers.

Formula (3) is not an alternative for estimating the degree of mixing, but allows one to obtain an integral estimate of the proportions of local and foreign material.

Sources of funding: The work was done under the GEOKHI RAS state assignment.

References:

Fassett C.I., Head J.W., Smith D.E., Zuber M.T., Neumann G.A. (2011) Thickness of proximal ejecta from the Orientale Basin from Lunar Orbiter Laser Altimeter (LOLA) data: Implications for multi-ring basin formation. Geophys. 38, L17201.

Housen K.R., Schmidt R.M., Holsapple K.A. (1983) Crater ejecta scaling laws: fundamental forms based on dimensional analysis. J. Geophys. Res. Solid Earth 88, 2485–2499.

Ivanov M.A., Head J.W., Hisenger H. (2023) New insights into the regional and local geological context of the Luna 16 landing site. Icarus 400, 115579.

Korotev R.L. (1997) Some things we can infer about the Moon from the composition of the Apollo 16 regolith. Meteor. and Planet. Sci. 32(4), 447–478.

Lucey P.G. (2004) Mineral maps of the Moon. Geophys. Res. Lett. 31, L08701.

McGetchin T.R., Settle M., Head J.W. (1973) Radial thickness variation in impact crater ejecta: implications for lunar basin deposits. Earth and Planet. Sci. Lett. 209(2), 226–236.

Oberbeck V.R., Hörz F., Morrison R.H., Quaide W.L., Gault D.E. (1975) On the origin of the lunar smooth-plains. The Moon 12, 19–54.

Petro N.E., Pieters C.M. (2006) Modeling the provenance of the Apollo 16 regolith. J. Geophys. Res. 111, 1–13.

Pike R.J. (1974) Ejecta from large craters on the Moon: Comments on the geometric model of McGetchin et al. Earth and Planet. Sci. Lett. 23(3), 265–271.

Sharpton V.L. (2014) Outcrops on lunar crater rims: Implications for rim construction mechanisms, ejecta volumes and excavation depths. J. Geophys. Res. Planets 119, 154–168.

Malyshev D.G., Ivanov M.A. Evolution of central-type volcanism on Venus (preliminary results)

[1]Vernadsky Institute of Geochemistry and Analytical Chemistry, Russian Academy of Sciences (GEOKHI RAS), Moscow, Russia (malyshev@geokhi.ru)

Abstract. This study aims to develop objective criteria for the classification and differentiation of volcanoes and coronae on the surface of Venus using machine learning techniques. Unlike existing approaches based on manual analysis of topographic profiles and diameters, we propose employing a variational autoencoder (VAE) for feature extraction followed by clustering. The methodology involves collecting and preprocessing radar imagery data from the Magellan mission, training the VAE, and applying clustering algorithms (K-means, DBSCAN) to identify subclasses of geological structures. The results of this work can be used to automate the analysis of Venus' surface and aid in preparations for future missions.

Keywords: *Venus, volcanoes, coronae, variational autoencoder, clustering, machine learning, SAR imagery.*

Introduction. The classification of geological features on the surface of Venus remains a critical challenge in planetary science. The primary data source is radar imagery acquired by the Magellan spacecraft (1990–1994), which covered 98% of the planet's surface [1]. These data revealed over 1,700 large volcanic structures, with particular attention given to coronae and volcanoes [2].

Despite decades of research, there are still no rigorous, objective criteria to distinguish coronae from volcanoes. Existing classifications rely either on topographic profiles (for coronae) [3–5] or parameters such as diameter and height (for volcanoes) [2, 6, 7]. This study aims to develop a new classification system for coronae and volcanoes by utilizing a comprehensive set of parameters derived from imagery and topography, as well as identifying novel, objective discriminative features using machine learning methods.

Study objects: Large and medium-sized volcanoes, as well as coronae on the surface of Venus, documented in Magellan radar imagery.
Unlike previous studies employing classifiers and manual methods, we use a variational autoencoder (VAE) for feature extraction, enabling the incorporation of a broader range of parameters and improving analytical accuracy. Additionally, our methodology includes clustering, which may reveal new subclasses of volcanoes and coronae.

Literature Review Earlier applications of machine learning to Venusian SAR imagery primarily focused on detecting small volcanoes. Studies [8, 9] utilized PCA and YOLO algorithms but were limited by data noise and scarce annotated datasets.

Autoencoders, particularly variational autoencoders (VAEs), are gaining traction for feature extraction and clustering tasks. The work in [10] introduced Deep Autoencoder Clustering (DAC), which enhances K-means performance through learned representations. Research [11] demonstrates that VAEs can cluster visually similar images without labels by transforming latent space with t-SNE [12], effectively separating classes. The approach in [13], where VAEs classified astronomical time-series images, further supports their utility for complex, noisy data analysis.
Prior clustering of Venusian volcanic constructs employed probability density functions (PDF) [14, 15] and machine learning methods like DBSCAN [6]. These studies produced spatial clusters of volcanic centers based on coordinates.

Research Objectives In this work, we maximize parameter utilization. The VAE is expected to extract more informative features than conventional methods, improving clustering quality and the separation of volcanoes and coronae. The resulting clusters may provide insights into the evolutionary history of volcanic centers on Venus.

Data As previously mentioned, the data used in this study consist of radar images acquired during the Magellan mission. We compiled a dataset from the following sources:

- Coronae: 446 images from [4, 5];
- Large volcanoes: 136 images, including 16 ambiguous structures (potential coronae) [6, 7];
- Medium-sized volcanoes: 106 images [6].

All images were supplemented with topographic data.

Each full-resolution image (4096×3839 pixels) was divided into 512×512 tiles, yielding 44,032 fragments (similarly for topography). These were combined into dual-channel (SAR + topography) inputs. Data augmentation included 90° rotations, reflections, and flips.

At this stage, the dataset was not split into training/validation/test subsets, as the focus was on testing the model's ability to reconstruct original images. However, future steps will adopt an 80-20 train-test split.

Methodology Initially, we trained a U-Net-based autoencoder [16], but its computational demands proved prohibitive. We then implemented a Vanilla VAE from [17], adapting its architecture for our data.

Architecture: Encoder compresses input images into a latent representation (feature vector) through successive downsampling. Outputs two vectors: μ (mean values), $log\sigma^2$ (logarithm of variance) of the latent distribution. Reparameterization trick: Samples

latent vectors from a normal distribution:

$$z = \mu + \sigma \cdot \epsilon, \epsilon \sim N(0, 1). \quad (1)$$

The decoder reconstructs the original image from the latent vector z, effectively learning to generate outputs that closely match the input data. Through this process, the model achieves two key objectives:

1. Accurate Reconstruction: Minimizing pixel-wise differences (e.g., MSE loss) between input and output images.
2. Latent Space Regularization: Encouraging the latent distribution to approximate a standard normal (via KL divergence), ensuring the space is structured and interpretable.

Implications for Feature Extraction:

- The compressed latent representation (z) captures discriminative features (e.g., topographic patterns, morphologic textures) essential for clustering.
- By training the VAE to reconstruct SAR-topography pairs, the model implicitly learns to prioritize geologically meaningful attributes over noise.

The loss function consists of two key components:

1) Reconstruction Loss (MSE), measures the pixel-wise difference between the input image x and reconstructed output $\hat{x}$:

$$L_{recon} = \|x - \hat{x}\|^2 \quad (2)$$

2) Kullback-Leibler Divergence (KLD), quantifies the divergence between the learned latent distribution and a standard normal distribution:

$$L_{KLD} = -\frac{1}{2}\sum(1 + \log\sigma^2 - \mu^2 - \sigma^2) \quad (3)$$

The total loss function combines these terms with experimentally determined weights:

$$L_{total} = \alpha \cdot L_{recon} + \beta \cdot L_{KLD}, \quad (4)$$

where $\alpha = 0.95$ and $\beta = 0.05$.

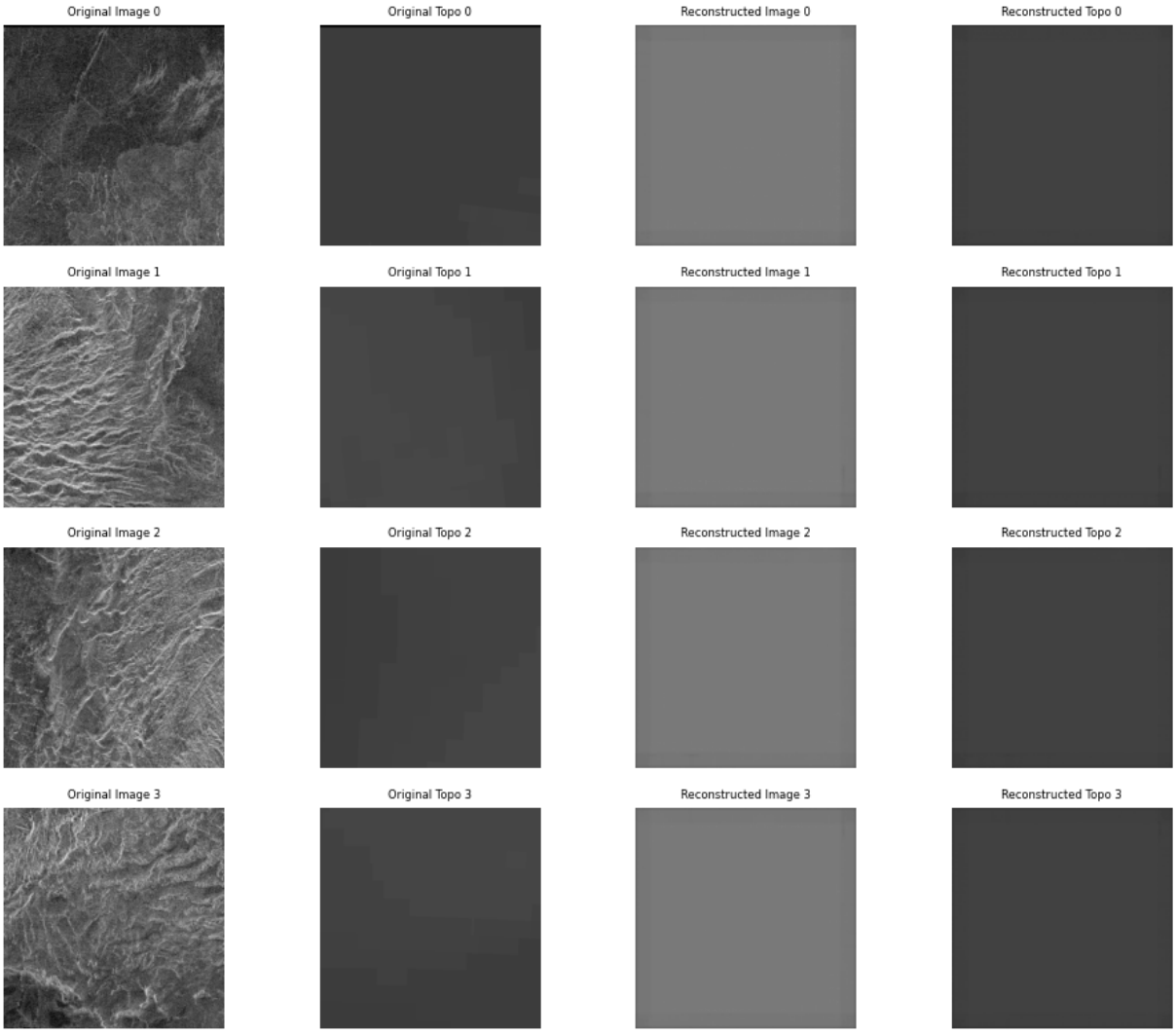

Fig. 1. The result of image generation by the autoencoder. The first two columns represent the original images and topography, the third and fourth are the result of reconstruction.

Experimental Framework. We conducted systematic experiments evaluating: different latent space dimensionalities, alternative loss functions, regularization approaches.

Clustering Methodology. For cluster analysis, we employ the Silhouette Coefficient (Equation 5):

$$s = \frac{b-a}{\max(a,b)} \quad (5)$$

where: a – mean intra-cluster distance (cohesion), b – mean nearest-cluster distance (separation). This metric provides quantitative assessment of: cluster compactness (how similar points are within clusters), cluster distinctness (how well-separated clusters are from each other). the coefficient ranges from -1 to 1, where: values approaching 1 indicate well-separated clusters, values near 0 suggest overlapping clusters, negative values may indicate incorrect clustering.

Results. At the current stage, the models do not demonstrate significant improvement in reconstruction quality. We conducted training experiments on the entire dataset using the VAE architecture described above for 20 epochs. The generated and original images are presented in Figure 1. Based on visual analysis, we decided not to continue training this model as it fails to provide adequate image reconstruction. The exact reasons for these results remain unclear, and we plan to continue experimenting with the model architecture while also performing additional data preprocessing to check for potential errors.

Conclusions. We have implemented and tested a variational autoencoder for the task of representing SAR images of the coronas and volcanoes of Venus. Despite the low quality of reconstruction at the current stage, the model shows potential as a tool for future clustering and the development of objective classification criteria. Work will continue towards improving the architecture and latent space analysis, with further clustering based on features derived from the VAE latent space.

Further experiments

Work on the following experiments is planned as the next steps:

1) Analysis of input data for artifacts and errors;
2) Modifications of the autoencoder architecture;
3) Selection of hyperparameters and regularization;
4) Conducting clusterization of the latent space and its visualization.

Funding: *The study was carried out under the State Assignment of the Vernadsky Institute of Geochemistry and Analytical Chemistry of the Russian Academy of Sciences*

References

1 Magellan Mission summary / R.S. Saunders, A.J. Spear, P.C. Allin [et al.] // J. Geophys. Res. – 1992. – Vol. 97, № E8. – P. 13067–13090.

2 Volcanoes and centers of volcanism on Venus / L.S. Crumpler, J.C. Aubele, D.A. Senske, S.T. Keddie, K.P. Magee, J.W. Head // In: Bougher, S.W., et al. (Eds.), Venus II: Geology, Geophysics, Atmosphere, and Solar Wind Environment. Tucson, AZ: University of Arizona Press. – 1997. – pp. 697–756.

3 Guseva E.N. Structures of Coronae on Venus: Results of Topographic and Geologic Analysis / E.N. Guseva, M.A. Ivanov // Solar System Research. – 2020. – Vol. 54, № 6. – P. 497–503.

4 Global Distribution and Characteristics of Coronae and Related Features on Venus: Implications for Origin and Relation to Mantle Processes / E.R. Stofan, V.L. Sharpton, G. Schubert [et al.] // J. Geophys. Res. – 1992. – Vol. 97, № E8. – P. 13347–13378.

5 Coronae on Venus: Morphology and origin / E.R. Stofan, V.E. Hamilton, D.M. Janes, S.E. Smrekar // In: Bougher, S.W., et al. (Eds.), Venus II: Geology, Geophysics, Atmosphere, and Solar Wind Environment. Tucson, AZ: University of Arizona Press. – 1997. – pp. 931–967.

6 Hahn, R. M., Byrne, P. K. A morphological and spatial analysis of volcanoes on Venus // Journal of Geophysical Research: Planets. – 2023, № 128, e2023JE007753. https://doi.org/10.1029/2023JE007753.

7 Ivanov M.A. Large volcanoes on Venus: Morphology, morphometry, and stratigraphy / M.A. Ivanov, J.W. Head // Icarus. – 2025. – Vol. 429, 116404.

8 Learning to Recognize Volcanoes on Venus / M.C. Burl, L. Asker, P. Smyth [et al.] // Machine Learning. – 1998. – Vol. 30. – P. 165–194.

9 Localization and Classification of Venusian Volcanoes Using Image Detection Algorithms / D. Đuranovic, S. Baressi Šegota, I. Lorencin, Z. Car // Sensors. – 2023. – Vol. 23, 1224.

10 Lu, S., Li, R. (2022). DAC–Deep Autoencoder-Based Clustering: A General Deep Learning Framework of Representation Learning. In: Arai, K. (eds) Intelligent Systems and Applications. IntelliSys 2021. Lecture Notes in Networks and Systems, vol 294. Springer, Cham. https://doi.org/10.1007/978-3-030-82193-7_13

11 Kovalenko A., Demyanenko Y. Image clustering by autoencoders // Information Technology and Nanotechnology – 2019 – p. 243-249. 10.18287/1613-0073-2019-2391-243-249.

12 https://scikit-learn.org/stable/modules/generated/sklearn.manifold.TSNE.html

13 Semenikhin T.A. Neural network architecture for artifacts detection in ZTF survey // Systems and Means of Informatics – 2024 – V. 34, № 1. – P. 70-79.

14 Edgardo C.-T. Insights into the dynamics of planetary interiors obtained through the study of global distribution of volcanoes II: Tectonic implications from Venus. // Journal of Volcanology and Geothermal Research. – 2014. – V. 281. – P. 70–84.

15 Edgardo C.-T. Magmatic-volcanic clusters and subclusters in Venus: Tectonic implications. // Earth-Science Reviews. – 2024. – V. 252, 104750.
16 Ronneberger O. U-Net: Convolutional Networks for Biomedical Image Segmentation. / Ronneberger, O., Fischer, P., Brox, T. // In: Navab, N., Hornegger, J., Wells, W., Frangi, A. (eds) Medical Image Computing and Computer-Assisted Intervention – MICCAI 2015. MICCAI 2015. Lecture Notes in Computer Science. – 2015. – V. 9351. https://doi.org/10.1007/978-3-319-24574-4_28
17 Subramanian A.K. (2020). PyTorch-VAE. GitHub repository. Retrieved from https://github.com/AntixK/PyTorch-VAE

Maxe L.P. Morphological analysis of fragments: object, explosion, iron bolide hypothesis. *UDC 524-1/-8*

ALC «STRIM», Mogilev, Belarus,
larissa_maxe@rambler.ru

Abstract. A morphological analysis of fragments of an object that exploded in the atmosphere was carried out on the basis of a database provided in digital form also various information characterizing the fragments, including scientific researches of meteorites. An eyewitness observed a bright, glowing object that flew at high speed until the explosion and fragments flew low above the surface. The data provided by him showed that the fragments are similar in composition and visually are similar to meteorites, but have differences. The results of supersonic destruction and synthesis processes are recorded in the shapes and macro relief of the fragments. It is noted that ultrafast critical load caused localized viscoplastic shift and manifestation of superplasticity of meteoritic iron. The author proposed the hypothesis of an iron bolide connecting it with the destroying of planetesimals in past. The scientific value of the fragments of the bolide is noted, the explosion of it is recorded in shapes, macro relief, and impressions of shock wave structures on the magnetite crust of the fragments.

***Keywords**: fragments; iron bolide; superplasticity; shock wave structures.*

Introduction. Billions of years ago, the destruction of planetesimals led to the formation of asteroids, which, entering the Earth's atmosphere after a long cosmic evolution, become bright iron bolides. Asteroids can be destroyed not only as a result of collisions, but also by the tidal gravitational influence of planets. Captured by the Earth's gravitational field, moving into a rendezvous orbit, asteroids become meteoroids. Entering the Earth's atmosphere at hyper- and supersonic speeds, they complete their cosmic evolution in a few seconds, sometimes tens of seconds by complete ablation in the atmosphere (meteors) or partial with falling of the remaining part to the surface (meteorites), occasionally global catastrophes occur. Before reaching the surface, large bright meteoroid fireballs often explode in the atmosphere.

An eyewitness observed the explosion of an object similar to a fireball over a desert area in 2008. At an angle to the horizon, the movement of a brightly glowing object from west to east was accompanied by a cone of a green spiral behind it. Ten years later, an eyewitness to the event (hereinafter referred to as the Searcher) began searching for and collecting fragments of the exploded object. In the collection collected by the Searcher, some of the stones stand out visually, but there are no fragments with regmaglypts among them. Density, shape, relief features, and a shiny black surface are the characteristics by which the Searcher selected fragments for its collection, connecting them to the explosive event it observed.

With a number of questions in addition to information about the event itself, a digital database of fragments selected by Searcher himself was sent to the author of this article (hereinafter referred to as the author). By Searcher himself, also was provided information about the observed event and digital materials (images, test data) the Searcher allowed it to be used in scientific publications. The amount of information about the explosion that the Searcher observed and the fragments it collected turned out to be sufficient to raise the question of the origin of the object, the nature of the explosion, as well as to conduct an targeted analysis of the data of that part of the fragments information about which was provided to author. Based on the volume, type and forms of the data provided and the results of his own information search, the author set a goal: to conduct an interdisciplinary morphological analysis of fragments of the explosion of the object, to propose a hypothesis of the origin and explosion of the object.

Objects. Method

The initial shape and material composition of the exploded object are unknown. Currently, fragments and samples collected by Searcher himself cannot be transferred to the author or other interested parties for research (that is not excluded in the future). Based on the amount of information received and additionally collected, to achieve the purpose of the work, the author used the method of morphological analysis, for which digital images, satellite images, laboratory test results, Searcher readings, and research results in the field of analysis tasks were included in the database.

Morphological analysis of fragments.

In this work an information review and morphological analysis of the data were carried out, taking into account the fact that the fragments of the object could be either industrial, terrigenous (for example – telluric iron) or extraterrestrial in origin. The fragments were divided into three groups according to their data. The first group included

fragments with traces of viscoplastic flow and fracture on one side, characteristic of metals and alloys subjected to severe force loading (stretching, torsion). The second group contains fragments corresponding to the type of rock fragmentation that occurs when rocks are destroyed by an explosion. The third category includes fragments with signs of spreading during fusion, Fig. 1.

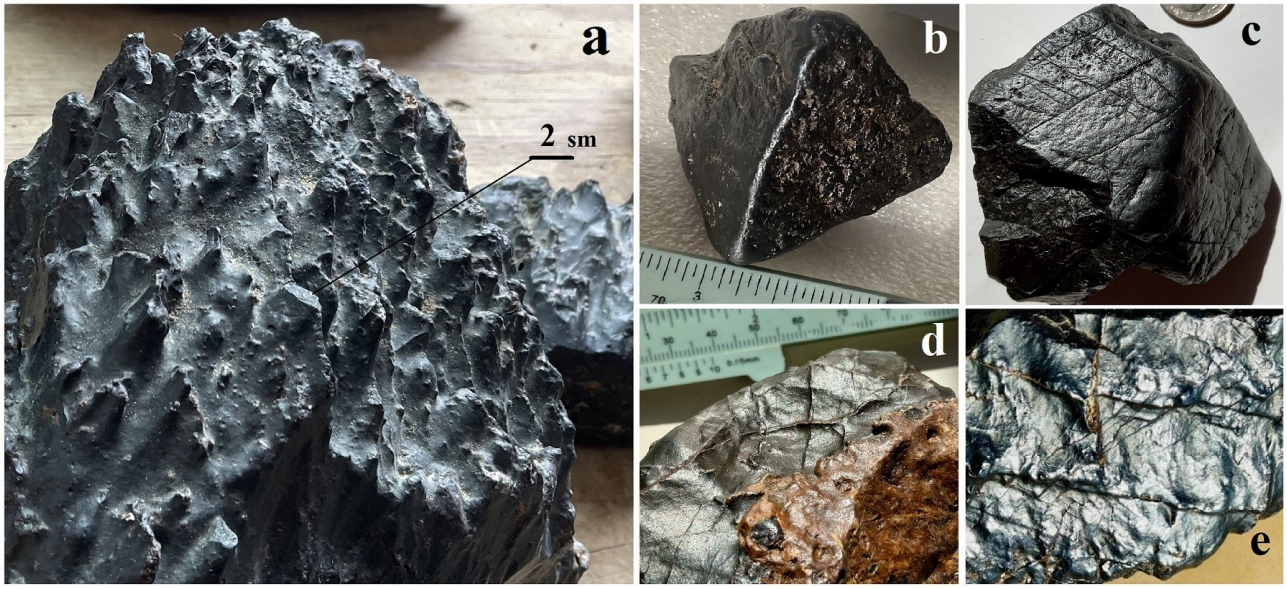

Figure 1. a – fragment of the first group with traces (cones) of viscoplastic fracture; b, c – fragments of the second group, destroyed like to the monolithic rock type; d – fragment of the third group, that has visible hardened "molten flow" after the fusion and two thin rhombic figure; e – stripes-cuts (depressions) on the black sparkly crust melted before, that forming rhombic picture.

The black sparkly fusion crust (thin crust after oxidizing iron surface) is present on the fragments of all three groups, but it has some differences. A thin matte crust covers cones and pits – macro relief projections on one side of the fragment of the first group, Fig. 1 a. A thin, black, shiny crust evenly covers the fragments of the second group from all sides, Fig. 1 b, c. On the third group fragment on the black crust there were appear influxes, Fig.1 d. On the Fig.1 e is shown a fragment with thin black crust that has the rhombic picture on surface created by "specific" cuts.

The Searcher provided data from an express analysis of the elemental composition and the values of some physic characteristics of the fragments, but without reference to a specific fragment. The density of fragments measured by the Searcher turned out to be similar and was less a little bit than the density of iron meteorites, he noted a very high metal strength of fragments taken to obtain flat sections. The Searcher did not observe the classic Widmanstatten structures (possible by incorrect processing), when measuring the electrical conductivity and magnetic properties of the thin black crust similar to magnetite, it noted anomalies. In addition, the Searcher found that some fragments have their own magnetic field. Such fragments may acquire special scientific value if they turn out to be meteorites, since magnetic meteorites form only in a magnetic field. The presence of a magnetic field in asteroids originating from planetesimals, as well as the appearance of a magnetic field in meteorites, has a scientific explanation (Maurel et al., 2020, Zhang, Bercovicia, 2023).

Damages that occur in places where the continuity of the material is disrupted by loading exceeding its strength limit have characteristic features. The macro relief of the fragments of the first group visualizes the fact and indicates destruction under the influence of strong stretching and/or torsion. Smooth indentations-pits, elongated upward and slightly obliquely truncated cones are located on one side of the fragment, Fig. 1 a. It is presumably that effect of deforming forces on the object began at the stage of approaching the planet and intensified in the atmosphere during deceleration, rotation, and fluctuations in bottom pressure. When approaching the surface, in some dynamically loaded part of the object, there was a sharp transition to the region of structural superplasticity, many zones of localization of superplasticity appeared, with the formation of a characteristic narrowing (neck) in each zone. The discontinuity occurred instantly as all necks of the superplastic flow broke off. By rapid cooling in the atmosphere, the breakage of the necks is fixed in the form of cones Fig. 1 a. Microcrystalline alloys of many metals have the property of superplasticity,

including meteoritic iron, that is a nickel–iron alloy (Perevezentsev and Svirina, 1998, Sharifullina et al., 2018).

A complex fracture of superplastic metal with bending and torsion rupture divided it into parts, in which the destruction continued, but in a different way. The ultrafast, probably supersonic, development of the crack network determined the type of destruction of the torn part of the object with monolitic rock-type fragmentation (Morozov et al., 2015). When analyzing the shapes a fact was noted: the vertices of some fragments (the second group) were "gently cut off" by a depression in the shape of a spherical segment (3 – 5 cm in diameter).

On the surface on the black crust of many fragments there are straight, narrow bands-cuts – depressions (sometimes elevations), which form rhombic figures ("diamonds") at the intersection, Fig. 1 a, b – d. The narrow profile of the cuts indicates that the cuts were exerted on a thin layer of magnetite in the plastic state. In powerful explosions, the initial velocity of fragments (shells, shell fragments, rock fragments) is supersonic. Accordingly, the velocity of the fragments that crossed the plasma stream that flowed around the object until its explosion was supersonic. The laws of supersonic aerodynamics limit the interaction and chemical reactions zone to a narrow near wall layer. Consequently, during the explosion of the object, the oxidation of iron with the formation of a thin crust – a thin layer of magnetite – proceeded in the mode of plasmodynamic synthesis (PDS) (Zimmerman et al., 2022). Due to the high rate of the exothermic oxidation reaction, heat exchange is limited, which leads to heating of the metal, so the fragments (from the second group) have smooth rounded edges and vertices. In contrast to the inflating of the cavity inside during the formation of magnetite microspheres (during PDS, welding, and ablation of meteoroids), in the PDS reaction, which flows superfastly around the fragment and closes on itself, the oxide is first formed – Fe_2O_3, which, by giving oxygen to iron, forms a Fe_3O_4 magnetite layer (rapidly cooling in the atmosphere till chrystallization). It is fact the exploded object "patented" a method for producing magnetite in the form of a thin coating on fragments, rather than in the form of hollow microspheres as in industrial PDS (Zimmerman et al., 2022).

Taking into account the supersonic motion of the object in the plasma cocoon and then its low-altitude explosion, the bands-cuts as rhombic on the magnetite crust can be considered as morphological imprints of shock wave structures formed by action of compaction jumps. This means that the stripes-cuts creating rhombic structures represent a "natural" visualization of supersonic flows, that is fixing chemically and physically on the freshly synthesized magnetite surface (Znamenskaya, 2021). The Searcher found also micro crystals similar to minerals of impact origin in the bands-cuts of the magnetite crust, which also indicates the shock synthesis and once more on uniqueness of the fragments.

The "preparedness" of the object. The features of the shapes and macro relief of the fragments suggest that the occurrence of forces that caused the metal to rupture may be due to both the composition of the object and high degree of its "preparedness" for destruction. Asteroids "reassembled" by gravity from remnants and fragments of planetesimals, asteroid debris, ice and dust can be destroyed more easily than others. After experiencing the effect of the tidal gravitational forces of the planets, large asteroids can split into fragments that continue to collide as they rotate, and sunlight can accelerate their rotation (the Yarkovsky effect). An asteroid with a metal part, attracted by gravity into the Earth's orbit, enters a convergence trajectory, guided with and by the center of mass and changing its rotational dynamics (Voropaev et al., 2020, Lobanova, Melnikov, 2024). Upon entering the atmosphere, the object becomes a fireball, being subjected to internal shear stresses caused by braking ablation of a part of the substance also increased pressure at the end face and bottom vacuum, shocks may be added to rotation. It is obvious that the moment of the object's approach to the surface, an ultrafast, critical deformation in object's body led to the appearance of a region of localization of plastic shear – localized adiabatic shear. Since this is an ultrafast local cycle involving plastic deformation of the material, the transition of work to heat, and thermal softening, the meteoritic iron inner the object, possessing structural superplasticity, was "ready" for local fracture under critical conditions (Perevezentsev, Svirina, 1998 Sharifullina et al., 2018).

The Iron bolide hypothesis. The hypothesis of “Iron bolide” proposed by the author is based on the results of a morphological analysis of the data provided by the Searcher and also on a comprehensive analysis of modern scientific data in the field of the set goal. Scientists believe that the presence of a part of the protoplanetary core in the asteroid that has undergone complete or even partial differentiation of matter lead to its own magnetism, while the "parents" of asteroids with melted and cooled metal, achondritic silicate and chondritic layers may be different parts of long-collapsed planetesimals (Maurel et al., 2020, Zhang, Bercovicia, 2023). The explosion and destruction of the iron bolide – object which Searcher observe, was preceded by the cosmic evolution of the asteroid, which could inherit or acquire the substance of the

planetesimal, in which case the bolide, in addition to the metal fragment, could include a "fragment" of the silicate mantle, which was undergone ablation in the atmosphere and could be dropped further by the explosion. The impact of the Earth's tidal forces changed the evolution of the bolide, destructive deformations during movement in the atmosphere eventually led to an explosion. When approaching the surface, the "bottleneck" between the iron "head" of the bolide and its mantle "tail", pierced by frozen veins of iron, could be affected by multidirectional deformation forces, creating a torsion moment, and they could be complemented by the factor of aerodynamic instability.

Conclusions. The fragments collected and selected by the Searcher and analyzed by author represent only a part of the evidence of the event – the explosion of an iron bolide, and they have scientific value exceeding commercial value. The results of supersonic processes, and processes both destruction and synthesis, were fixed in the shapes and macro relief of the fragments of the bolide. The macro-relief of the fragments shows the property of superplasticity of meteoritic iron which was fixed in the cones of adiabatic shear as a consequence of destruction. Most of the fragments are coated with magnetite, which was formed in the plasma of the bolide itself during the PDS process. As it cooled, the magnetite formed an uncial crust in which the imprints of shock wave structures were fixed. Fragments of this rare iron bolide must be preserved without damage in order to be transferred to a specialized national organization for research.

The author expresses his gratitude to the anonymous Searcher who provided the data and allowed it to be used in scientific publications.

References

Lobanova K.S., Melnikov A.V. On the effect of asteroid deformations in close proximity to the Earth on its rotational and orbital dynamics. Proceedings of the Main Astronomical Observatory in Pulkovo, № 235. P. 30-43. doi:10.31725/0367-7966-2024-235-30-43.

Maurel Clara, Bryson James F. J., Lyons Richard J., Ball Matthew R., Chopdekar Rajesh V., Scholl Andreas, Ciesla Fred J., Bottke William F., Weiss Benjamin P. Meteorite evidence for partial differentiation and protracted accretion of planetesimals. Sci. Adv. 2020; 6. P. 1-9.

Morozov V.A., Savenkov G.G., Barakhtin B.K., Lukin A.A., Gunko Yu.F., Rudometkin K.A. Crack velocity under superfast loading. Letters to the JTP, 2015, Vol. 41, issue 3, P. 26-32.

Perevezentsev V.N., Svirina Yu.V. High-speed superplasticity of microcrystalline alloys under conditions of local melting of boundaries. Journal of Technical Physics. 1998, Vol. 68, № 12, P. 38-42.

Sharifullina E.R., Schweikin A.I., Trusov P.V. Review of experimental studies of structural superplasticity: evolution of the microstructure of materials and mechanisms of deformation // Bulletin of the Perm National Research Polytechnic University. Mechanics. – 2018. – № 3. – P. 103-127. DOI: 10.15593/perm.mech/2018.3.11.

Voropaev S.A., Django Yan, Barriot Jean-Pierre. Rupture of an elongated small body by tidal forces of the Earth during approach: possible scenarios. Astronomical Bulletin, 2020, T 54, № 2, P. 171-182.

Zhang Zhongtian, Bercovicia David. Generation of a measurable magnetic field in a metal asteroid with a rubble-pile core. PNAS 2023, Vol. 120, № 32. P. 1–8. https://doi.org/10.1073/pnas.

Zimmerman A.I., Shanenkov I.I., Sivkov A.A., Ivashutenko A.S., Nasyrbaev A.R., Vlasov V.A. Investigation of the effect of the type of inert gas on the process of plasmodynamic synthesis of iron oxides. News of the Russian Academy of Sciences. Physical series, 2022, volume 86, № 10, P. 1479-1485.

Znamenskaya I. Methods of panoramic visualization and digital analysis of thermophysical fields. Review // Scientific visualization. 2021. 13. № 3. C. 125-158. URL: http://svjournal.org/2021-3/13/?lang=ru.

Shornikov S.I., Yakovlev O.I. Condensation parameters of perovskite as the least volatile compound of CAIs matter.

V. I. Vernadsky Institute of Geochemistry & Analytical Chemistry RAS, Moscow sergey.shornikov@gmail.com

Abstract. Thermodynamic data on perovskite obtained by the Knudsen effusion mass spectrometric method in the temperature range of 1791–2441 K are considered. The presented information can be used to evaluate the *pT*-conditions of CAIs matter condensation in the outer shell of a star before its explosion or during the explosion and expansion of gas and condensate.

***Keywords**: Ca-Al-inclusions of chondrites, evaporation, Knudsen effusion mass spectrometric method*

Many researchers adhere to the traditional view that Ca-Al-inclusions of chondrites (CAIs) were formed by condensation of a Solar composition gas in the immediate vicinity of the young Sun (Grossman, 1972; Grossman et al., 2000). According to an alternative point of view CAIs were formed during the condensation of stellar gas outside and long before the formation of the Solar nebula (Cameron, Lodders, 2004) during the expansion of gas and condensate (dust) during the explosion of a *TP-AGB* (Terminally Pulsating Asymptotic Giant Branch) type Supernova (Sahijpal, Soni, 2006) or an oxygen-rich star type the White Dwarf Star (Meyer, Bermingham, 2020). From the observation data of isotopic anomalies in CAIs, it follows that stellar matter was thrown into the protosolar system in the form of gas and condensate, which left a memory of

short-lived isotopes (^{26}Al, ^{41}Ca, ^{60}Fe, ^{107}Pd). It is also assumed that it is possible to deliver stellar refractory minerals from a white dwarf star to a protosolar nebula (Meyer, Bermingham, 2020) and, in particular, perovskite as a carrier of nonradiogenic isotopes of ^{48}Ca and ^{50}Ti (Dauphas et al., 2014).

$CaTiO_3$ perovskite evaporation from a Knudsen effusion molybdenum cell was studied by mass spectrometry in the temperature range of 1791–2441 K (Shornikov, 2019, 2019a, 2020). The mass spectrometer MI-1201 was equipped with a modified ion source for high-temperature studies (up to a temperature of 3000 K). The design of the developed ion source and the methodological features of experiment were described in detail earlier (Shornikov et al., 2000).

The established molecular composition of the gas phase over perovskite (Shornikov, 2019) indicated the perovskite evaporation with the formation of a vapor species by reaction:

$$[CaTiO_3] = (CaTiO_3), \quad (1)$$

further dissociation of which led to the formation in the gas phase of a significant number of atomic and molecular species typical of simple oxides (Ca, CaO, Ti, TiO, TiO_2, O, O_2):

$$(CaTiO_3) = (CaO) + (TiO_2) \quad (2)$$
$$(CaO) = (Ca) + (O) \quad (3)$$
$$(TiO_2) = (TiO) + ½(O_2) \quad (4)$$
$$(TiO) = (Ti) + (O). \quad (5)$$

Based on the partial pressures (p_i) of vapor species obtained under reducing conditions, the oxide activities (a_i) in perovskite were calculated (Shornikov, 2019a) according to the following ratios (Lewis, Randall, 1923):

$$a_{CaO} = \frac{p_{CaO}}{p^\circ_{CaO}} - \frac{p_{Ca}\,p_O}{\nu^\circ_{Ca}\,\nu^\circ_O} \quad (6)$$

$$a_{TiO_2} = \frac{p_{TiO_2}}{p^\circ_{TiO_2}} - \frac{p_{TiO}\,p_O}{\nu^\circ_{TiO}\,\nu^\circ_O}, \quad (7)$$

where p_i and p_i° are the partial pressures of the vapor species over perovskite and simple oxide. The equilibrium partial pressures and concentrations (x_i) of the vapor species over perovskite were determined and given in Table 1. The thermodynamic data used in the calculations for reactions (3) – (5) were taken from (Glushko et al., 1978–1982).

Table 1. Partial pressures and concentrations of vapor species over perovskite.

Vapor	Partial pressure p_i, atm			Concentration x_i, mol			$x_{i,\,2400}$ /
specie	1800 K	2241 K	2400 K	1800 K	2241 K	2400 K	$x_{i,\,1800}$
O	6.25×10^{-10}	8.38×10^{-7}	5.98×10^{-6}	3.0×10^{-1}	1.5×10^{-1}	1.7×10^{-1}	0.6
O_2	2.64×10^{-11}	5.84×10^{-8}	4.87×10^{-7}	1.3×10^{-2}	1.1×10^{-2}	1.4×10^{-2}	1.1
Ca	6.10×10^{-10}	5.57×10^{-7}	3.05×10^{-6}	2.9×10^{-1}	1.0×10^{-1}	8.6×10^{-2}	0.3
CaO	2.47×10^{-13}	1.83×10^{-9}	1.80×10^{-8}	1.2×10^{-4}	3.3×10^{-4}	5.1×10^{-4}	4.3
Ti	2.25×10^{-15}	1.67×10^{-10}	2.12×10^{-9}	1.1×10^{-6}	3.0×10^{-5}	6.0×10^{-5}	56
TiO	3.73×10^{-11}	4.75×10^{-7}	3.80×10^{-6}	1.8×10^{-2}	8.6×10^{-2}	1.1×10^{-1}	6.1
TiO_2	8.05×10^{-10}	3.58×10^{-6}	2.20×10^{-5}	3.8×10^{-1}	6.5×10^{-1}	6.2×10^{-1}	1.6
$CaTiO_3$	4.87×10^{-15}	3.58×10^{-9}	7.74×10^{-8}	2.3×10^{-6}	6.5×10^{-4}	2.2×10^{-3}	945

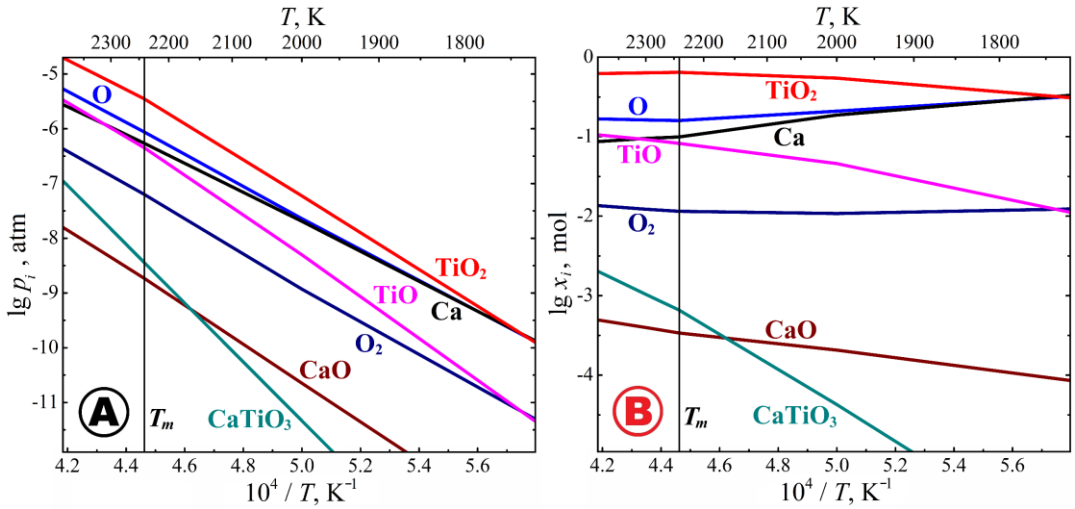

Fig. 1. Dependences of the logarithm of the partial pressures (A) and the mole fractions (B) of the vapor species over perovskite vs. the reverse temperature.

The thermodynamic data on perovskite obtained under equilibrium conditions can be used to evaluate the *pT*-conditions of CAIs matter condensation in the outer shell of a star before its explosion or during the explosion and expansion of gas and condensate. In particular, at 2200 K (that is slightly lower than the melting point of perovskite, equal to 2241 K), the partial pressures of the dominant vapor forms are (atm): $p(TiO_2) = 2.17\times10^{-6}$; $p(O) = 5.05\times10^{-7}$; $p(Ca) = 3.18\times10^{-7}$; $p(TiO) = 2.55\times10^{-7}$; the partial vapor pressure of stoichiometric gaseous perovskite $p(CaTiO_3) = 1.28\times10^{-9}$ atm (Fig. 1A). It should be noted that the stability of the $CaTiO_3$ gaseous molecule, which increases with increasing temperature (Fig. 1B), can serve as confirmation of the hypothesis of joint delivery of neutron-rich anomalous isotopes of ^{48}Ca and ^{50}Ti in one compound (carrier mineral).

***Financing**: The study was performed within the framework of the state assignment of the Vernadsky Institute of Geochemistry & Analytical Chemistry of the Russian Academy of Sciences.*

References

Cameron A. G. W., Lodders K. (2004) Interpretation of the meteoritic extinct radioactivity – mean life relation. *Lunar & Planet. Sci. Conf*., Abs. № 1181.

Dauphas N., Chen J. H., Zhang J., Papanastassiou D. A., Davis A. M., Travaglio C. (2014) Calcium-48 isotopic anomalies in bulk chondrites and achondrites: evidence for a uniform isotopic reservoir in the inner protoplanetary disk. *Earth & Planet. Sci. Lett*., vol. 407, pp. 96–108.

Glushko V. P., Gurvich L. V., Bergman G. A., Veitz I. V., Medvedev V. A., Khachkuruzov G. A., Yungman V. S. (1978–1982) Thermodynamic properties of individual substances. Moscow, Nauka.

Grossman L. (1972) Condensation in the primitive solar nebula. *Geochim. Cosmochim. Acta*, vol. 36, № 5, pp. 597–619.

Grossman L., Ebel D. S., Simon S. B., Davis A. M., Richter F. M., Parsad N. M. (2000) Major element chemical and isotopic compositions of refractory inclusions in C3 chondrites: the separate roles of condensation and evaporation. *Geochim. Cosmochim. Acta*, vol. 64, № 16, pp. 2879–2894.

Lewis G. N., Randall M. (1923) Thermodynamics and the free energy of chemical substances. N. Y. and London, McGrow-Hill book comp., 676 p.

Meyer B. S., Bermingham K. R. (2020) Exploding white dwarf stars and the carriers of nucleosynthetic isotope anomalies. *Lunar & Planet. Sci. Conf*., Abs. № 2326.

Sahijpal S., Soni P. (2006) Stellar nucleosynthetic contribution of extinct short-lived nuclei in the early solar system and the associated isotopic effects. *Met. & Planet. Sci*., vol. 41, № 6, pp. 953–976.

Shornikov S. I., Archakov I. Yu., Chemekova T. Yu. (2000) A mass spectrometric study of vaporization and phase equilibria in the Al_2O_3–SiO_2 system. *Russ. J. Phys. Chem*., vol. 74, № 5, pp. 677–683.

Shornikov S. I. (2019) Mass spectrometric investigation of evaporation processes of perovskite. *Russ. J. Phys. Chem. A*, vol. 93, № 6, pp. 1024–1031.

Shornikov S. I. (2019a) High temperature mass spectrometric study of thermodynamic properties of $CaTiO_3$ perovskite. *Russ. J. Phys. Chem. A*, vol. 93, № 8, pp. 1428–1434.

Shornikov S. I. (2020) Study of CaO–TiO_2 melts by Knudsen effusion mass spectrometry. *Russ. J. Phys. Chem. A*, vol. 94, № 7, pp. 1289–1299.

Shpekin M.I.[1], Ferreyra R.T.[2], Shishkina V.S.[1] Shock wave processes on the Moon on the Aitken crater example.

[1] Kazan Federal University, Kazan MichaelS1@yandex.ru shshkna13@yandex.ru
[2] National University of Argentina, Cordoba ricardo.tomas.ferreyra@unc.edu

The Aitken crater in the central part of the Moon's reverse hemisphere is known for the fact that images of this crater were taken from lunar orbit by the Soviet spacecraft “Zond-6” and “Zond-8” in 1968 and 1970 and delivered to Earth for the first time in the history of space research. An important distinguishing feature of this survey is that it was carried out with a long-focus metric camera on large-format film, and the film itself was processed in a laboratory on Earth. The listed features of this survey made it possible to obtain high image quality, and the calibrated cameras of the named spacecraft were provided high measuring properties of the delivered images.

Another important characteristic of Aitken crater is its advantageous selenographic position. The crater was formed as a result of an impact event right on the edge of the vast lowlands of the far side of the Moon. This lowland, named by the authors of its discovery the "Southwestern lowland" [1-5], as further research showed, turned out to be a giant impact crater, and this crater itself was the central part of a large impact multi-ring basin, which was named the "South Pole - Aitken"(SPA). It should be noted that the above names of the lowland and the basin are unofficial names of these objects [6].

The authors of numerous publications have already addressed the study of the Aitken crater. For example, a photogrammetric network of lunar coordinates was built at TsNIIGAiK covering a section of the equatorial zone of the far side of the Moon in the longitude range from the Orientale Mare to the Aitken crater [7]. This network was subsequently condensed on the territory of Aitken and its surroundings [8]. LTO [9, 10] topographic maps of 1:100,000 scale were built on two sheets on

the sites of Aitken crater and its surroundings based on images from the Apollo spacecraft obtained in 1971 and 1972 by their crews. The territory of the Aitken crater was used as a kind of polygon for comparing the heights of lunar relief elements found by the method of orbital photogrammetry and the method of orbital laser altimetry [8]. The high quality of the orbital images from the Zond and Apollo spacecraft made it possible to begin studying the crater by building 3D-models of the crater itself, as well as its selected elements. So to the authors [11,12] was manage to use 3D modeling technology to study the relief of the central peak (CP) of the crater and, in particular, for the first time to detect a glacier-like tongue "creeping out" from the southwestern slope of the central response to the bottom of the crater and examine its structure. In [13] the elements of the relief of the crater to the east of its central peak in the area of the so-called "bulbous fields" were studied. As a result of the survey of the mentioned area, a small crater was found on the bottom of the Aitken crater (D=4.3) with an unusual structure. The authors of the noted publication concluded that the impactor of this crater could be a slow asteroid, whose energy was enough to penetrate into the lava lake Aitken to a depth of 2-4 km. But it was not enough to lead to the formation of an explosive process with significant heating of the substance at the point of contact and the release of the substance around the crater.

Another direction in the study of the Aitken crater is related to the assessment of the age of the lunar surface. The authors of the 2011 publication [14], based on the analysis of the planets of the Solar System, showed that the age of the Moon and the age of the lunar surface should be considered as two significantly different categories. If the age of the Moon itself counts from its birth and the value is constant in its meaning, then the age of the lunar surface, as well as various territories on the Moon, depends on the activity of shock processes, the intensity of which varies with time. The named dependence is presented in the most detailed way within the framework of the Galactocentric paradigm outlined in the monographs [15, 16]. Thus, in [17], the consequences of the mentioned paradigm are considered in relation to the formation of the modern appearance of the Moon and, in particular, estimates of the age of the impact craters Aitken and Tsiolkovsky, as well as estimates of the volume of residual water in these two craters brought by icy comet nuclei during periods of periodic bombardment are given. As part of this approach, the largest crater of the Moon associated with the “South Pole – Aitken” basin is also considered. Estimates of the age of this unique formation indicate that the named basin represents one of the youngest impact structures on the Moon. There is only one large impact basin younger than the SPA basin. This is the Orientale Mare and its multi-ring basin, which lie on the material of emissions from the SPA basin. Since the Aitken crater is located, as noted above, on the edge of the central part of the SPA basin, it is also younger in age than the basin itself and lies, like the Eastern Sea, on the material of emissions from the SPA basin.

The above circumstances make it even more attractive to study Aitken crater, as one of the most recent craters of this size on the Moon. The fact is that it is the fresh craters that contain more evidence of crater-forming events in the form of relief elements remaining in the crater to this day.

One of these elements is a glacier-like tongue in the southwestern part of the central peak (CP). Figure 1 shows a fragment of a 3D-model of the central peak in the area where the tongue is viewed on our model from the front side. Earlier in the publications [13, 18] we considered possible variants of the origin of the language, one of which is associated with shock waves provoked by shock waves which were formed 5 small craters east of the central peak in the area of "bulbous fields". The mentioned scenario assumes that the substance of the central peak was in the aggregate state at the time of impact, which was different from the state of a solid body. Such an option in the life of the crater is quite possible due to its youth. This is also indicated by the craters formed in the northern part of the central peak. Figure 2 shows a general view of the CP and its surroundings, and Figure 3 shows the position of three craters in the north of the CP. The state of the CP substance is clearly reflected in the nature of the relief formed on the crest of the crater rim in the center of the figure. Here, the surface structure gives the impression of a loose, porous, viscous material. There is not even a clear edge of the crater rim, which usually appears as a result of the impactor fall on a hard surface. That is, it is not possible to detect the crest of the shaft itself or the edge of the inner bowl of the crater. Such a character of the crater slopes can be expected in a young crater formed on fresh emission material. In this case, these are fresh emissions from the SPA basin, on the edge of which the Aitken crater was formed. The material capacity of the emissions themselves from the central part of the SPA can be estimated and the authors express the hope to carry out such calculations. This calculation may be of practical interest from the point of view of the physics of the formation of the central peak, which is formed by the response shock conical wave [19], and subsequently the physics of the formation of the entire crater.

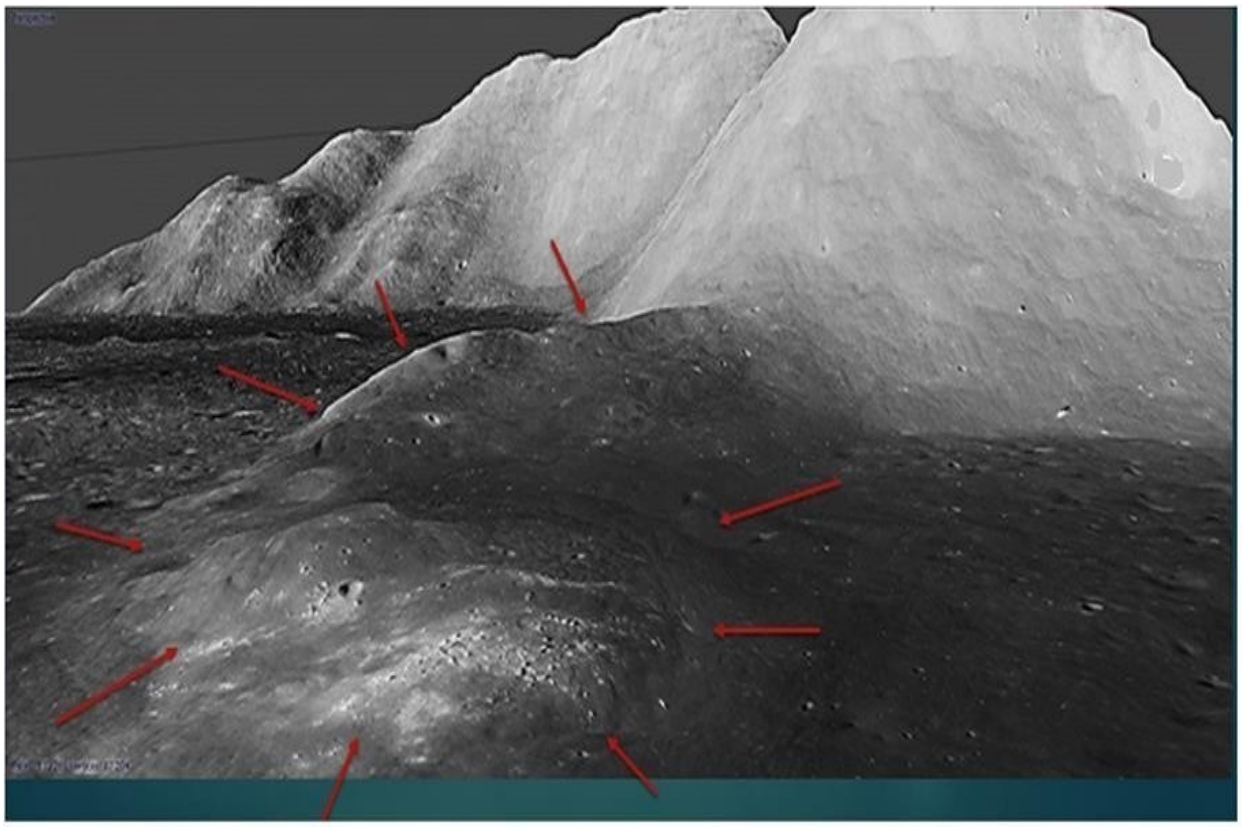

Figure 1. View of the "glacier-like tongue" on a fragment of the 3D-model built at Kazan Federal University [12] based on the orbital images of the Aitken crater, delivered to Earth by the crew of the “Apollo-17” spacecraft. The outline of the tongue is shown by the red arrows. The upper part of the drawing is occupied by the peaks of the central Aitken peak, which appear to be high mountains on the scale of the 3D-model. To the right and left of the tongue are dark areas of the Aitken floor, covered with small impact craters. The front part of the tongue contains many lunar boulders, which are confidently viewed on a high-resolution model.

Figure 2. View of the central part of the Aitken crater. In the center of the picture is the central hill of the crater, on the left are isolated mountain peaks, on the right is an area of “bulbous fields”.

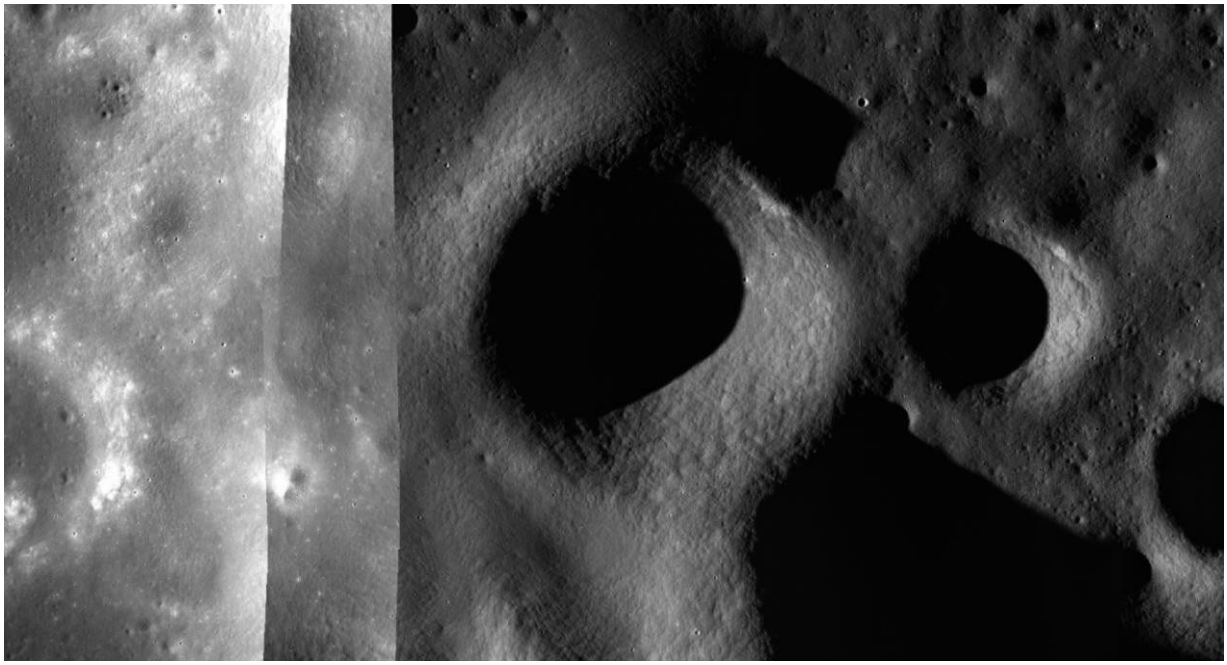

Figure 3. View of the position of three craters in the north of the Aitken CP. The state of the CP substance is clearly reflected in the nature of the relief formed on the crest of the crater rim in the center of the figure. Here, the surface structure gives the impression of a loose, porous, viscous material. There is not even a clear edge of the crater rim, which usually appears as a result of the impactor fall on a hard surface.

References:

1 B. Rodionov, I. Isavnina, Y. Avdeev, V. V. Blagov, et al., Preprint-41 IKI AN SSSR, 34, 1970.

2 B. N. Rodionov, I. V. Isavnina, Y. F. Avdeev, V. D. Blagov, et al., Kosm. Issled., 9, 450, 1971.

3 B. N. Rodionov, I. V. Isavnina, Y. F. Avdeev, V. D. Blagov, et al., Cosmic Research, 9, 410, 1971.

4 B. Rodionov, A. Nefed'ev, M. Shpekin, S. Valeev, and V. Kiselev, Kosm. Issled., 14, 624, 1976.

5 B. N. Rodionov, A. A. Nefedev, M. I. Shpekin, S. G. Valeev, and V. V. Kiselev, Cosmic Research, 14, 624, 1977.

6 Shpekin M.I. "South Pole — Aitken" basin from first measurements ("Zond-6", 1968) to first landing of the lunar rover ("Chang'e-4", 2019) // Scientific papers of the Institute of Astronomy of the Russian Academy of Sciences – 2020, Volume 5, pp. 157-162 — M.: Publishing house Janus-K. DOI: 10.26087/INASAN.2020.5.3.014

7 Aleksashin E.P., Timofeev Yu.S., Shirenin A.N. Selenocentric coordinate system Zond-8. Methods of construction and catalog of coordinates of reference points // Collection of scientific papers of the Central Research Institute of Geodesy, Aerial Photography and Cartography named after F. N. Krasovsky / [Editor L. M.Melnikov]. - M. : TsNIIGAiK, 1989. - 216 p.

8 Sitdikova R.A. Topographic survey of the Aitken crater on the far side of the Moon // Bachelor thesis Kazan — 2008 KAZAN STATE UNIVERSITY 48p.

9 ATKEN BOREALIS LTO86D4 Sheet 1 NASA Washington DC April 1976

10 ATKEN AUSTRALIS LTO104D1 Sheet 2 NASA Washington DC April 1976

11 Shpekin M.I., Sitdikova R.A. Topographical survey of Aitken crater on the far side of the Moon.Microsymposium 46 Vernadsky-Brown 2-3 October 2007, Moscow, Russia, Program and Abstracts, Abstract № 46-64. International Forum "Space: Science and Problems of the 21st century" dedicated to the 50th anniversary of the launch of the First artificial satellite of the Earth. October 1-5, 2007, Moscow – St. Petersburg.

12 Mukhametshin, Ch.R., Semenov, A.A., Shpekin, M.I. Experience of modeling relief of impact lunar crater Aitken based on high-resolution orbital images // Journal of Physics: Conference Series 2018,Том: 1015 Выпуск: 3, 7p.

13 Shpekin M. I., Salimov R. R., Semenov A. A. Orbital photogrammetry of selected relief elements with evidences of geological activity in Aitken crater on the far side of the Moon // IOP Conference Series: Earth and Environmental Science, Vladivostok, 06–09 октября 2020 года. – Vladivostok, 2021. – P. 062020. IOP Conf. Ser.: Earth Environ. Sci. 666 062020. 12 p. – DOI 10.1088/1755-1315/666/6/062020.

14 Barenbaum A.A., Shpekin M.I. About Age of the Lunar Surface. Proceedings of Annual Conference on Experimental Petrology, Mineralogy and Geochemistry April 19-20, 2011, Moscow, Russia, GEOKHI RAS. 5p. http://onznews.wdcb.ru/publications/v03/asempg11en/2 011NZ000141.pdf

15 Barenbaum A. A. Galaxy, Solar System, Earth. Subordinated Processes and Evolution Moscow: GEOS, 2002, 393 p. (In Russian).

16 Barenbaum A.A. Galactocentric paradigm in geology and astronomy. Moscow. PH:LIBROKOM, 2010, 546 p. (In Russian).

17 Наша статья с АА по остаточной воде в кратере Ц и Э на симпозиуме?

18 Shpekin M.I., Shishkina V.S. The structure features of young impact craters in the area of "bulbous fields" on the aitken crater floor // The fourteenth Moscow Solar System symposium 14M-S3 October 9-13, 2023. Space research institute of russian academy of sciences Moscow, Russia. Book of Abstracts pp. 143-145 ISBN: 978-5-00015-061-0
19 Ferreyra R. T., Shpekin M. I. A fluid dynamical model to shape complex craters XXXIV Intern. Conf. on Interaction of Intense Energy Fluxes with Matter (EOS-2019) Book of Abstracts, Moscow & Chernogolovka & Nalchik, March 1-6, (2019) 397 pages. ISBN 978-5-6040595-9-3.

Tselmovich V.A.[1], Kuzina D.M.[2], Muftakhetdinova R.F.[3], Yakovlev G.A.[3], Ezhov V.F.[4], Chetverikov O.Yu.[4], Bulat S.A.[3,4] The first detection of tin and copper particles in the magnetic component of space matter from Antarctica collected by a magnetic trap. *UDC 523. 3-1/-8*

[1] Borok State Research Institute of Physics of the Earth RAS tselm@mail.ru, tel.7(9066327448),
[2] Kazan Federal University, Kazan, Russia, di.kuzina@gmail.com
[3] Ural Federal University, Yekaterinburg, Russia, izrozka91@bk.ru
[4] National Research Center "Kurchatov Institute" – PNPI, Gatchina, Russia. bulatsergey28@gmail.com

Annotation. Antarctica is considered the best place to assess the amount and composition of cosmic matter arriving at Earth. The unique conditions of Antarctica make it possible to collect samples and determine the type and amount of cosmic and other particles that got into the sample during the sampling period. The result of dust collection depends on the conditions and time of collection, including the trap's design. Dust collection using a trap made of NdFeB magnets at the Vostok station was carried out from 27.12.2023 to 23.01.2024. The microstructure and composition of 132 particles were analyzed by microscopic methods at the Borok State University, UrFU, and KFU. Iron-containing (magnetic) particles of cosmic dust (CD) or micrometeorites (MM) were found in the samples, similar to the same particles previously found by many authors who isolated them from various objects. A feature of the particles we found in one of the samples was the content of tin (Sn) (in metallic and oxide forms) and (metallic) copper (Cu). Considering that Sn is extremely rare in meteorites, and there were multiple finds in the samples, we believe they may be of both meteoritic and technogenic origin.

Abstract. Antarctica is the best place to assess the amount and composition of incoming cosmic matter to Earth. The unique conditions of Antarctica make it possible to take samples and determine the type and amount of cosmic and other particles trapped in the sample during sampling time. The result of dust collection depends on the conditions and time of collection, including the trap's design. Dust collection using a trap from NdFeB magnets at Vostok station was carried out from 27.12.2023 to 23.01.2024. The microstructure and composition of 132 particles were analyzed by microscopic methods at Borok, UrFU, and KFU. Iron-containing (magnetic) particles of space dust (KP) or micrometeorites (MM) were found in the samples, similar to the same particles previously found by many authors who isolated them from various objects. The peculiarity of the particles we found in one of the samples was their content of tin (Sn) (in metallic and oxide forms) and (metallic) copper (Cu). Considering that Sn is extremely rare in meteorites, and the finds in the samples were multiple, we believe that they may be of both meteoritic and anthropogenic origin.

***Keywords**: Antarctica; NdFeB magnetic trap; cosmic dust; micrometeorites; technogenic substance; tin; copper; iron; electron microscopy*

Introduction. Meteorites are most often found in the Earth's deserts, including Antarctica, where two-thirds of meteorites have been found (Meteorite Bulletin Database, https://www.lpi.usra.edu/meteor/). Most finds are on glaciers that flow together with stones frozen into them, some of which remain at the foot of the mountains. Although Antarctica is ideal for collecting meteorites, modern micrometeorites are challenging to find in the ice, although a number of collections have already been created (Concordia and Fuji - van Ginneken M et al., 2024). The authors attempted to collect and record the CP and MM magnetic components using a trap made of NdFeB magnets. However, not all elements of the detected dust particles were ignored.

Materials and methods. On 27.12.2023, two NdFeB traps with monthly and annual exposures were installed to collect the CP and MM (Fig. 1a, b).

The traps were taken by snowmobile to the test site with coordinates 78.497824 S 106.748117 E, 4 km from the Vostok station, and installed on tripods at a distance from each other (Fig. 1a, b). The installation of the traps was carried out in clean clothes (put on-site) 50 meters upwind of the snowmobile stop. On January 23, 2024, one of the two assemblies (traps) was dismantled cleanly and sent to the R/V Akademik Treshnikov for delivery to the PPNPI NRC KI laboratory. The second trap was left for a year's exposure and was removed in February 2025 (delivery to St. Petersburg in May-June 2025). The samples were sent to the Borok State Research Institute of Physics of the Earth RAS (sample No. 5, installation height 1 m), UrFU (sample No. 4), and the Analytical Microscopy Interdisciplinary Center of Kazan Federal University (sample No. 3). The samples were analyzed using Olympus BX51M, Carl Zeiss Axiovert 40 MAT optical metallographic microscopes, FE-SEM ∑IGMA VP and Tescan Mira3 scanning electron microscopes, and a Merlin field emission scanning electron microscope from Carl Zeiss (Germany) equipped with an Aztec X-MAX elemental analysis detector.

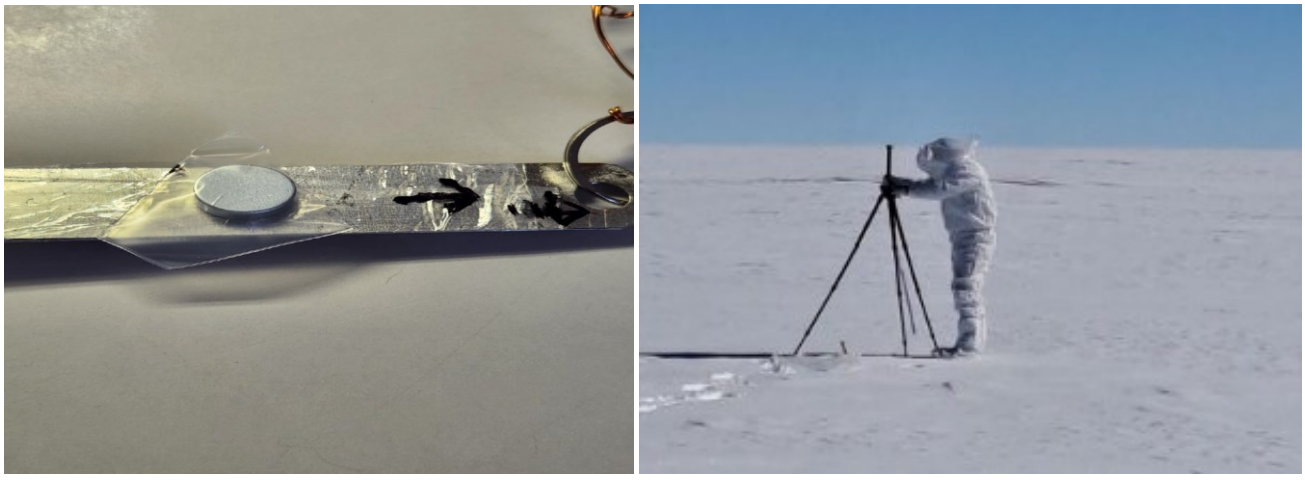

a) **b)**

Fig. 1. a) NdFeB magnet in a plastic bag - a trap for meteorites; b) installation of NdFeB magnets for collecting cosmic dust.

Discussion. When examining the dust particles found on the surface of NdFeB magnets, 132 particles ranging in size from 0.5 μm to 200 μm were found. 54 spectra were recorded from the particles most suitable for analysis using an energy-dispersive spectrometer, and the particle compositions were calculated.

The following components of the collected dust were identified:

1. Micrometeorites: particles of Fe-Ni alloys, kamacite, and taenite, Fig. 2a, 2b, Table 2a, 2b.

2. A component of a rare meteorite, or technogenic, particles of "pure" Sn and Cu (Fig. 3 a-d), Fe-Ti alloy.

3. Terrigenous component: particles of NaCl, presumably a component of sea salt aerosols (Fig. 4 a); particles of aluminosilicates, calcites, magnetite (Mt) (Fig. 4 b-c), quartz.

4. Background cosmic component: pure native Fe.

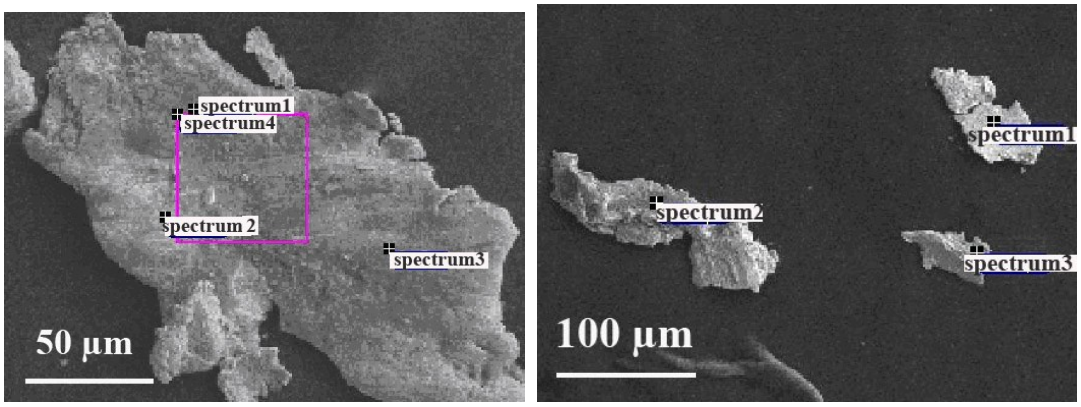

a) **b)**

Fig. 2. a) particles of micrometeorites (compositions are given in Table 1a); b) particles of Fe-Ni alloy and ferrous aluminosilicate (compositions are given in Table 1b).

Table 1a.

Spectrum	O	Mg	Si	Fe	Co	Ni	Total
Spectrum 1				57.81	0.78	41.42	100.00
Spectrum 2	1.38		0.28	72.73	1.30	24.32	100.00
Spectrum 3				88.32	2.17	9.51	100.00
Spectrum 4	5.26	2.97	1.89	60.93	0.97	27.98	100.00

Table 1b.

Spectrum	O	Na	Mg	Al	Si	S	Cl	Ca	Fe	Co	Ni	Total
Spectrum 1									92.17	2.13	5.71	100.0
Spectrum 2	25.7	3.64	11.78	0.71	16.31	2.60	1.43	3.26	32.68	0.63	1.27	100.0
Spectrum 3	17.5	0.86	9.36	0.66	6.87				40.19	0.58	24.02	100.0

Figures 2a and 2b show typical Fe-Ni micrometeorite particles and a particle of ferrous aluminosilicate (Fig. 2b, spectrum 2). Tables 1a and 1b show the particle compositions.

The discovered particles are similar to the previously described (Badyukov et al., 2018) fine-grained slag-like micrometeorites from the Novaya Zemlya collection - moderately heated during flight in the atmosphere, not remelted (underwent weak heating during braking in the atmosphere), while some of them retained their original structure. The similarity of morphology and composition of samples from the Arctic and Antarctic allows us to conclude that they have a single nature of origin and similar conditions of accumulation and preservation. The detection of Sn in the form of oxides, native Sn, and an alloy of Sn with Fe is unexpected and atypical. Tin is extremely rare in meteoritic matter, but it was found in alloys in ferrous meteorites (Wampler J. et al., 2020) and chondrites (Creech et al., 2019). Sn is a rare trace element; tin is the 47th most common element in the earth's crust. According to various sources, the Clarke content of tin in the earth's crust ranges from 2•10−4 to 8•10−3% by weight. The main Sn mineral is cassiterite (tin stone) SnO_2, containing up to 78.8% Sn. Minor Sn content is found in carbonaceous CI and CM chondrites (Alexander et al., 2013). Our findings suggest that the source of Sn and Cu may be either rare meteorites or destroyed electronic components of burnt-out satellites, the fall path of which, when they sank in the ocean, passes over Antarctica. We discovered six particles containing Sn in metallic or oxide form (however, we had not previously made such finds in Antarctica), in films on Fe (Fig. 3a-e, Table 2). In Fig. 4. terrigenous particles are shown: a) NaCl; b) $CaCO_3$, Mt (magnetite); c) detrital Mt with a Fe film.

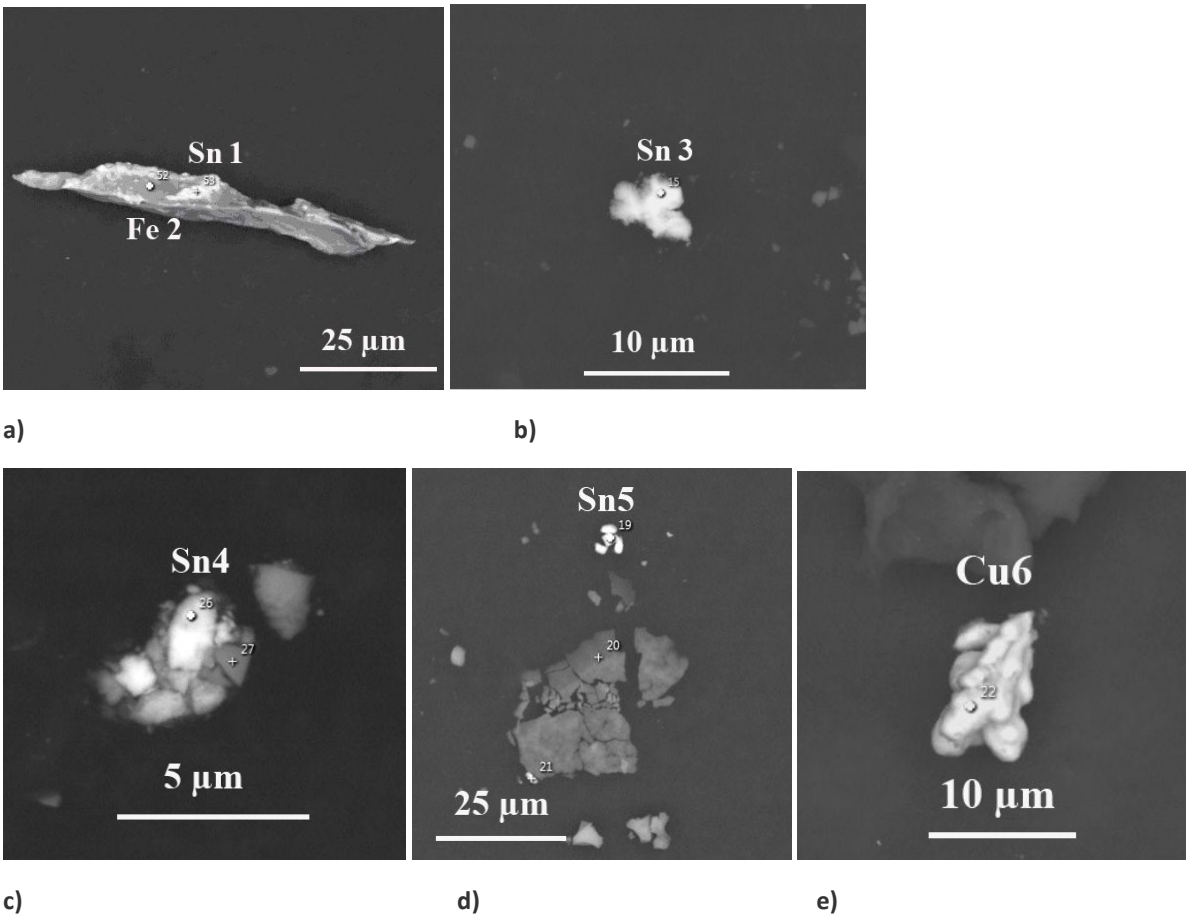

Fig. 3: a) - Sn films on Fe; c) - d - Sn in metallic and oxide form; e) Cu particle.

Table 2.

Spectrum	Al	O	Fe	Sn	Cl	Cu	**Total**
Spectrum Sn1	0.15	7.11	24.79	67.95	0.00	0.00	100.00
Spectrum Fe2	0.21	4.66	91.34	2.95	0.00	0.84	100.00
Spectrum Sn3	0.15	42.54	0.48	56.40	0.43	0.00	100.00
Spectrum Sn4	0.00	55.17	9.06	35.77	0.00	0.00	100.00
Spectrum Sn5	0.00	11.70	0.00	88.30	0.00	0.00	100.00
Spectrum Cu6	0.00	0.77	0.00	00.00	0.00	99.23	100.00

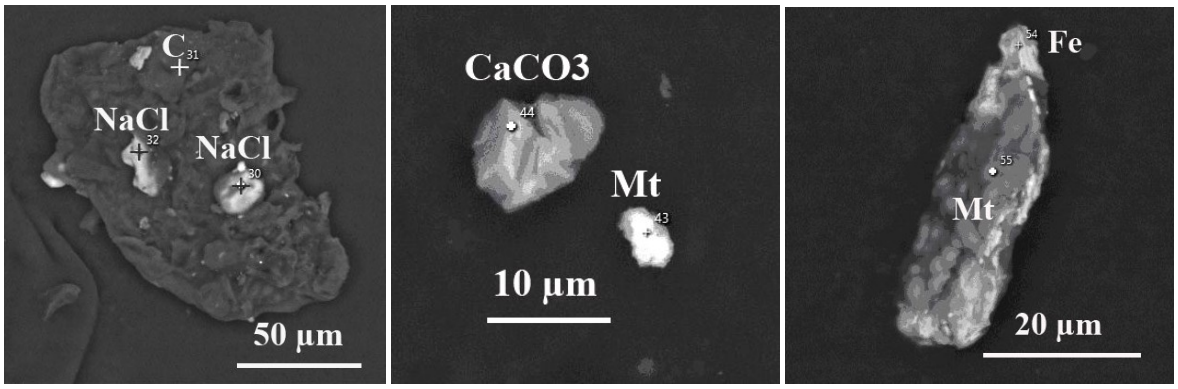

a) b) c)

Fig. 4. Terrigenous particles: a) NaCl; b) CaCO3, Mt (magnetite); c) detrital Mt with Fe film.

Conclusions. In the particles collected at the Vostok station in Antarctica using the NdFeB magnetic trap, particles of cosmogenic (Fe, FeNi), terrigenous (NaCl, $CaCO_3$, Mt), and rare cosmogenic or anthropogenic (Sn) origin, ranging in size from 0.5 to 200 µm in diameter, were identified. Studies of the particles on a magnetic trap with the head of the exposure will clarify the latter conclusion. If confirmed (tin isotope is needed), this will be the first find of tin in the magnetic fraction of the CP from Antarctica.

References

1. Badyukov D.D., Brandstätter F., Topa D. Fine-grained slag-like and unmelted micrometeorites: their sources and relationship with cosmic spherules //Geochemistry. -2015.- No. 11. - pp. 1026–1039. https://doi.org/10.1134/S0016702918110022
2. Alexander C.M.O.'D., Howard K.T., Bowden R., Fogel M.L The classification of CM and CR chondrites using bulk H, C and N abundances and isotopic compositions // Geochim. et Cosmochim. Acta. - 2013.- V. 123. P. 244–260.
3. Creech J.B. and F. Moynier. Tin and zinc stable isotope characterization of chondrites and implications for early //Solar System evolution, Chemical Geology. - 2019.- 511_81-90.
4. Ginneken Matthias, Penelope J Wozniakiewicz, Donald E Brownlee, Vinciane Debaille, Vincenzo Della Corte, et al.) Micrometeorite collections: a review and their current status // Philosophical Transactions of the Royal Society A: Mathematical, Physical and Engineering Sciences. -2024.- 382 (2273) - pp.20230195. ff10.1098/rsta.2023.0195ff. ffhal-04575591f
5. Wampler J., Thiemens M, Cheng S., Yimei Z., and Schullera I. Superconductivity found in meteorites. Proceedings of the National Academy of Sciences). - 2020.- No. 3 - DOI: 10.1073/pnas.1918056117